ARMY RESEARCH LABORATORY

Numerical Prediction of Supersonic Shock-boundary Layer Interaction

by Vishal A. Bhagwandin and James DeSpirito

ARL-TR-5602 **July 2011**

Approved for public release; distribution unlimited.

NOTICES

Disclaimers

The findings in this report are not to be construed as an official Department of the Army position unless so designated by other authorized documents.

Citation of manufacturer's or trade names does not constitute an official endorsement or approval of the use thereof.

Destroy this report when it is no longer needed. Do not return it to the originator.

Army Research Laboratory
Aberdeen Proving Ground, MD 21005

ARL-TR-5602 **July 2011**

Numerical Prediction of Supersonic Shock-boundary Layer Interaction

Vishal A. Bhagwandin and James DeSpirito
Weapons and Materials Research Directorate, ARL

Approved for public release; distribution unlimited.

REPORT DOCUMENTATION PAGE

Form Approved
OMB No. 0704-0188

Public reporting burden for this collection of information is estimated to average 1 hour per response, including the time for reviewing instructions, searching existing data sources, gathering and maintaining the data needed, and completing and reviewing the collection information. Send comments regarding this burden estimate or any other aspect of this collection of information, including suggestions for reducing the burden, to Department of Defense, Washington Headquarters Services, Directorate for Information Operations and Reports (0704-0188), 1215 Jefferson Davis Highway, Suite 1204, Arlington, VA 22202-4302. Respondents should be aware that notwithstanding any other provision of law, no person shall be subject to any penalty for failing to comply with a collection of information if it does not display a currently valid OMB control number.
PLEASE DO NOT RETURN YOUR FORM TO THE ABOVE ADDRESS.

1. REPORT DATE *(DD-MM-YYYY)*
July 2011

2. REPORT TYPE

3. DATES COVERED (From - To)
November 2009 to January 2011

4. TITLE AND SUBTITLE
Numerical Prediction of Supersonic Shock-boundary Layer Interaction

5a. CONTRACT NUMBER

5b. GRANT NUMBER

5c. PROGRAM ELEMENT NUMBER

6. AUTHOR(S)
Vishal A. Bhagwandin and James DeSpirito

5d. PROJECT NUMBER
AH80

5e. TASK NUMBER

5f. WORK UNIT NUMBER

7. PERFORMING ORGANIZATION NAME(S) AND ADDRESS(ES)
U.S. Army Research Laboratory
ATTN: RDRL-WML-E, B4600
Aberdeen Proving Ground, MD 21005

8. PERFORMING ORGANIZATION REPORT NUMBER
ARL-TR-5602

9. SPONSORING/MONITORING AGENCY NAME(S) AND ADDRESS(ES)

10. SPONSOR/MONITOR'S ACRONYM(S)

11. SPONSOR/MONITOR'S REPORT NUMBER(S)

12. DISTRIBUTION/AVAILABILITY STATEMENT
Approved for public release; distribution unlimited.

13. SUPPLEMENTARY NOTES

14. ABSTRACT
Shock-boundary layer interaction was numerically simulated via steady-state, Reynolds-averaged Navier-Stokes methods using CFD++, a general purpose fluid flow solver. The simulations emulated experiments performed in two wind tunnel facilities, the Institut Universitaire des Systèmes Thermiques Industriels Wind Tunnel and the University of Michigan Wind Tunnel. Typical flow characteristics were captured, such as the location of the incident and reflected shock waves, boundary layer recirculation and separation, and increase in boundary layer displacement and momentum thicknesses. The numerical velocity components and Reynolds stresses in the boundary-layer compared fairly well with experimental data; however, improvement is still needed. The sensitivity of the simulations to the choice of turbulence model and grid density was also demonstrated.

15. SUBJECT TERMS
Computational fluid dynamics, shock-boundary layer interaction

16. SECURITY CLASSIFICATION OF:

a. REPORT	b. ABSTRACT	c. THIS PAGE
Unclassified	Unclassified	Unclassified

17. LIMITATION OF ABSTRACT
UU

18. NUMBER OF PAGES
46

19a. NAME OF RESPONSIBLE PERSON
Vishal A. Bhagwandin

19b. TELEPHONE NUMBER (*Include area code*)
(410) 306-0731

Standard Form 298 (Rev. 8/98)
Prescribed by ANSI Std. Z39.18

Contents

List of Figures **iv**

List of Tables **v**

Acknowledgments **vii**

1. Introduction **1**

2. Simulation Methodology **3**

3. Results **8**

3.1 UFAST Wind Tunnel 8

3.2 UMICH Wind Tunnel 22

4. Summary and Conclusions **30**

5. References **32**

List of Symbols, Abbreviations, and Acronyms **34**

Distribution List **35**

List of Figures

Figure 1. Schematic showing the shock-boundary layer interaction in an internal flowpath (*9*). 1

Figure 2. UFAST wind tunnel flowpath. 3

Figure 3. UMICH wind tunnel flowpath. 3

Figure 4. UFAST computational domain: (a) full length view, ~20.4M cells, (b) 3-D grid detail in test-section, and (c) 2-D grid detail in test-section. Grids generated in Pointwise v16.04R1. Note: only half the geometry was gridded. 4

Figure 5. UMICH computational domain: (a) full length view, ~18M cells (b) 3-D grid detail in test-section, and (c) 2-D grid detail in test-section. Grids generated in Gambit v2.4.6. Note: only half the geometry was gridded. 5

Figure 6. Sample residual histories of the right-hand side equations: (a) UFAST – SST and (b) UMICH – SST. 7

Figure 7. Three-dimensional rendering of UFAST numerical flowfield for SST turbulence model showing Mach number contours on the tunnel symmetry plane and oil flow streamlines on the tunnel lower wall. 9

Figure 8. Transverse profile in the interaction zone showing centerline and corner SBLIs: (a) experimental SPIV data (*9*) on a plane 2 mm above the lower wall (scale units in mm), (b) CFD streamline data using SST turbulence model on a plane 2 mm above the lower wall (scale units in m), and (c) CFD streamline data using SST turbulence model on the lower wall (scale units in m). 9

Figure 9. Turbulence model comparison on symmetry plane: (a) u-velocity and (b) numerical Schlieren. 10

Figure 10. Experiment vs. CFD on symmetry plane in SBLI region: (a) u-velocity and (b) v-velocity. 11

Figure 11. Turbulence model sensitivity: u-velocity axial profiles on the symmetry plane in the SBLI region. 12

Figure 12. Turbulence model sensitivity: v-velocity axial profiles on the symmetry plane in the SBLI region. 13

Figure 13. Turbulence model sensitivity: $u'v'$ axial profiles on the symmetry plane in the SBLI region. 14

Figure 14. Grid sensitivity: (a) u-velocity and (b) v-velocity symmetry plane contours in SBLI region, SST model. 15

Figure 15. Grid sensitivity: u-velocity axial profiles on the symmetry plane in the SBLI region, SST model. 16

Figure 16. Grid sensitivity: v-velocity axial profiles on the symmetry plane in the SBLI region, SST model. 17

Figure 17. Grid sensitivity: u′v′ axial profiles on the symmetry plane in the SBLI region, SST model. 18

Figure 18. Pressure contours on the lower wall for the (a) full grid and (b) mirrored half grid, SST model. 19

Figure 19. Spanwise profiles of pressure, skin friction and velocity using full grid, X=0.20 m, SST model. 20

Figure 20. Spanwise profiles of pressure, skin friction and velocity using full grid, X=0.32 m, SST model. 21

Figure 21. Spanwise profiles of pressure, skin friction and velocity using full grid, X=0.40 m, SST model. 22

Figure 22. Three-dimensional rendering of UMICH numerical flowfield showing Mach number contours on the tunnel symmetry plane and oil flow streamlines on the tunnel lower wall, SST model, 7.75º case. 23

Figure 23. Turbulence model comparison on symmetry plane: (a) u-velocity and (b) numerical Schlieren, 7.75º case. 24

Figure 24. Experiment vs. CFD on symmetry plane in SBLI region: (a) u-velocity and (b) v-velocity. 25

Figure 25. Turbulence model sensitivity: u-velocity axial profiles on the symmetry plane in the SBLI region. 26

Figure 26. Turbulence model sensitivity: v-velocity axial profiles on the symmetry plane in the SBLI region. 27

Figure 27. Effect of shock-generator wedge angle on the test section flowfield – symmetry plane numerical contours of: (a) Mach number and (b) numerical Schlieren. Plots are in mm. 29

Figure28. Effect of shock-generator wedge angle on the SBLI: Mach number numerical contours on the symmetry plane near the lower wall. Plots are in mm. 30

List of Tables

Table 1. Test cases for SBLI workshop. 2

Table 2. Summary of simulation parameters. 6

INTENTIONALLY LEFT BLANK.

Acknowledgments

The authors would like to acknowledge the organizers and participants of the American Institute of Aeronautics and Astronautics (AIAA) Shock Boundary Layer Interaction (SBLI) Workshop held in Orlando, Florida, on 8 January 2010, for provision of experimental data and intellectual input on the current subject. This work was supported in part by a grant of high-performance computing time from the U.S. Department of Defense (DoD) High Performance Computing Modernization Program at the ARL DoD Supercomputing Resource Center, Aberdeen Proving Ground (APG), Maryland.

INTENTIONALLY LEFT BLANK.

1. Introduction

The aerospace community has significant interest in the accurate numerical prediction of shock-boundary layer interaction (SBLI) using computational fluid dynamics (CFD). SBLI occurs in both external and internal aerodynamic problems, including flow over airfoils, wings, rotors, ballistic projectiles, turbomachinery blades, and high-speed inlets and combustors. To facilitate the design and analysis of such aerospace systems, the SBLI phenomena must be isolated, modeled, and studied.

Figure 1 provides a simple illustration of SBLI on a wind tunnel wall induced by supersonic flow over a flat plate. When the supersonic flow encounters the leading edge of the plate, a shock wave propagates towards the lower wall where it interacts with the boundary layer, inducing an abrupt pressure gradient. Capturing detailed flow physics—such as the location of incident shock wave, boundary layer recirculation and separation, increase in boundary layer displacement and momentum thicknesses, corner flow influence, and unsteadiness of the reflected shock wave, among others—has proven to be a challenge (*1, 7–10, 15, 19, 22*).

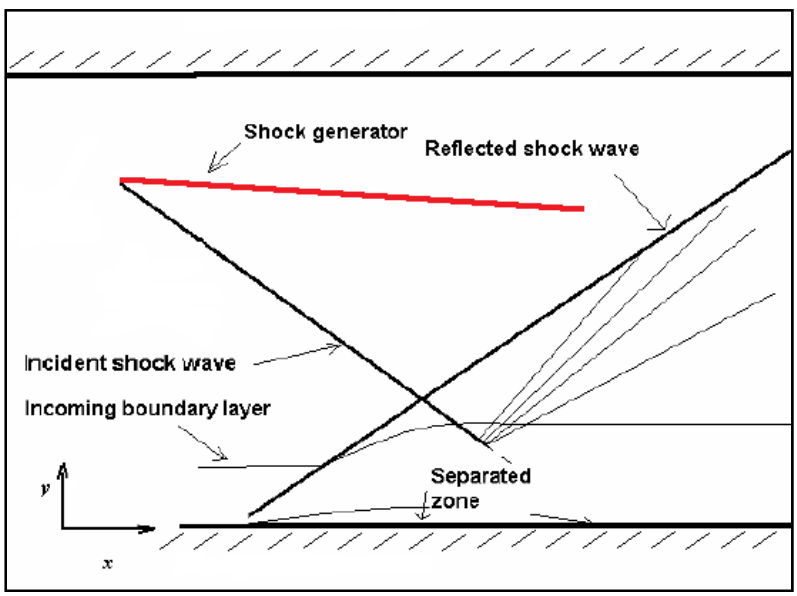

Figure 1. Schematic showing the shock-boundary layer interaction in an internal flowpath (*9*).

Recognizing the need to study SBLI, the U.S. Air Force Research Laboratory (AFRL) hosted a workshop in January 2010 at the AIAA Aerospace Sciences Meeting in Orlando, Florida, where current high-fidelity physics-based computational methods were assessed for prediction of SBLI phenomena (*3, 4, 6, 13*). While the impetus of the workshop was to study SBLI in relation to inlets for supersonic vehicles, SBLI is also of interest to the U.S. Army Research Laboratory

(ARL) in the study of external aerodynamics of supersonic projectiles and missiles. A variety of computational approaches was presented at the SBLI Workshop to include Reynolds-averaged Navier-Stokes (RANS) methods; Large Eddy Simulation (LES); hybrid RANS/LES, structured, unstructured, and adaptive gridding techniques; various upwind numerical schemes; and various turbulence models.

An experimental database for comparison purposes was derived from two wind tunnel facilities, viz, (i) the Institut Universitaire des Systèmes Thermiques Industriels Wind Tunnel (IUSTI) in Marseille, France (this data was furnished by UFAST (*4, 9*), a European Union consortium sponsoring SBLI research); and (ii) the University of Michigan Wind Tunnel (UMICH) (*4, 14*), working with the Collaborative Center for Aeronautical Sciences (CCAS).

The experimental database was comprised of four SBLI test cases—one from UFAST and three from UMICH. Table 1 summarizes these test cases. Results for all four cases were presented by the authors at the SBLI Workshop. For case 1, additional simulations and analyses were completed following the workshop; for case 2, no additional simulations, only further analyses, were completed.

Table 1. Test cases for SBLI workshop.

Case #	Mach	Shock Generator Angle	Data Source
1	**2.25**	**8.0**	**UFAST**
2	**2.75**	**7.75**	**UMICH**
3	**2.75**	**10.0**	**UMICH**
4	**2.75**	**12.0**	**UMICH**

Figure 2 shows a 2-D schematic of the UFAST wind tunnel, in which supersonic flow at Mach 2.25 (test case 1) is delivered to a 122.1 mm × 170 mm (height × span) test section where a flat plate shock generator is located. The flow is fully turbulent as it approaches the test section with a boundary layer thickness of about 10 mm. The plate is 4 mm thick, has a sharp leading edge, is inclined at 8º to the tunnel axis, and spans the width of a test section. The tunnel walls have a 0.28º divergence for a boundary layer correction. Streamwise particle image velocimetry (PIV) data for mean and fluctuating velocity components in the SBLI region was obtained on the tunnel centerline. Stereo-PIV (SPIV) data was also obtained on a plane 2 mm above and parallel to the tunnel lower wall.

Figure 3 shows a 2-D schematic of the UMICH wind tunnel, in which supersonic flow at Mach 2.75 is delivered to a 70 mm × 57 mm (height × span) test section where a wedge-shaped shock generator is located. The flow is fully turbulent as it approaches the test section with a boundary layer thickness of about 10 mm. The wedge is centered in the test section, supported by a strut, and spans half the tunnel. The bottom wall of the wedge is inclined at 7.75º, 10º, and 12º (test cases 2, 3, and 4) to the tunnel axis. SPIV data for mean and fluctuating velocity components was obtained on the centerline streamwise plane and several spanwise planes in the SBLI region.

SPIV inflow data was also obtained on two planes upstream of the SBLI region, one providing core flow data and the other boundary layer data.

All simulations used steady-state, RANS methods and were conducted using a CFD++ v8.1.1 flow solver—a commercial fluid flow solver by Metacomp Technologies, Inc (*18*). The effect of several turbulence models was investigated. The influence of grid resolution on the results was also addressed.

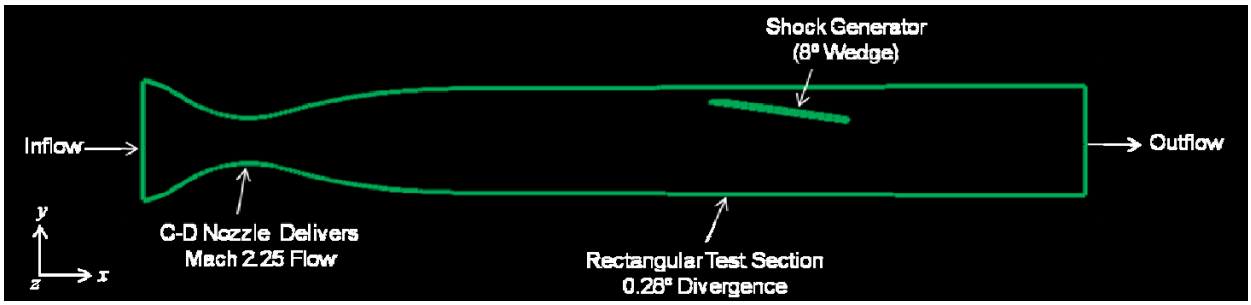

Figure 2. UFAST wind tunnel flowpath.

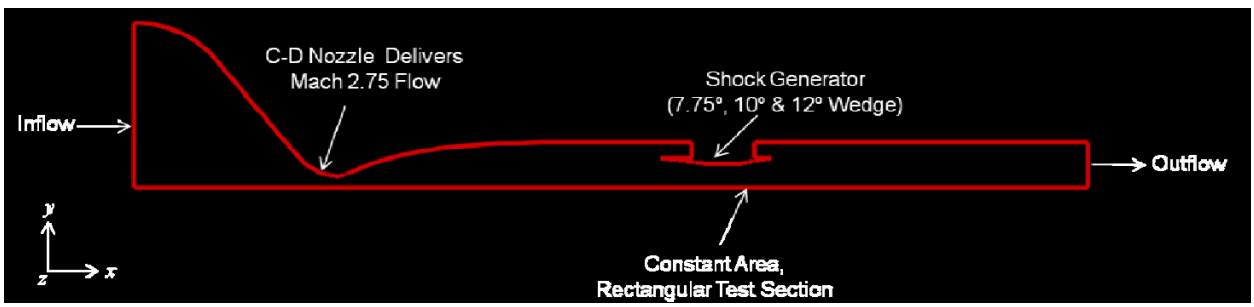

Figure 3. UMICH wind tunnel flowpath.

2. Simulation Methodology

The computational domains were three-dimensional and consisted of half the wind tunnel geometries, since they were symmetrical about the vertical centerline plane (or z=0 plane). The UFAST and UMICH computational domains, respectively, consisted of 20.4M and 18.0M structured, hexahedral cells generated using Pointwise v16.04R1 and Gambit v2.4.6 (see figures 4 and 5). The UMICH grid additionally contained prism elements to facilitate gridding between the half-span shock generator and the tunnel side wall. To capture wall boundary layer effects, the initial grid wall spacing was 5×10^{-6} m (0.005 mm) in both cases. This ensured y+ values of less than 0.5 along the wind tunnel test section walls, and less than 1.0 otherwise, for compatibility with a solve-to-the-wall strategy. The UFAST and UMICH grids were decomposed for parallel processing on 136 and 120 processors, respectively. Computations were performed on "Harold," a SGI Altix ICE 8200 Supercomputer, and "MJM,"a Linux Networx Advanced

Technology Cluster, both housed and managed by the ARL DoD Supercomputing Resource Center (DSRC) at Aberdeen Proving Ground (APG), MD.

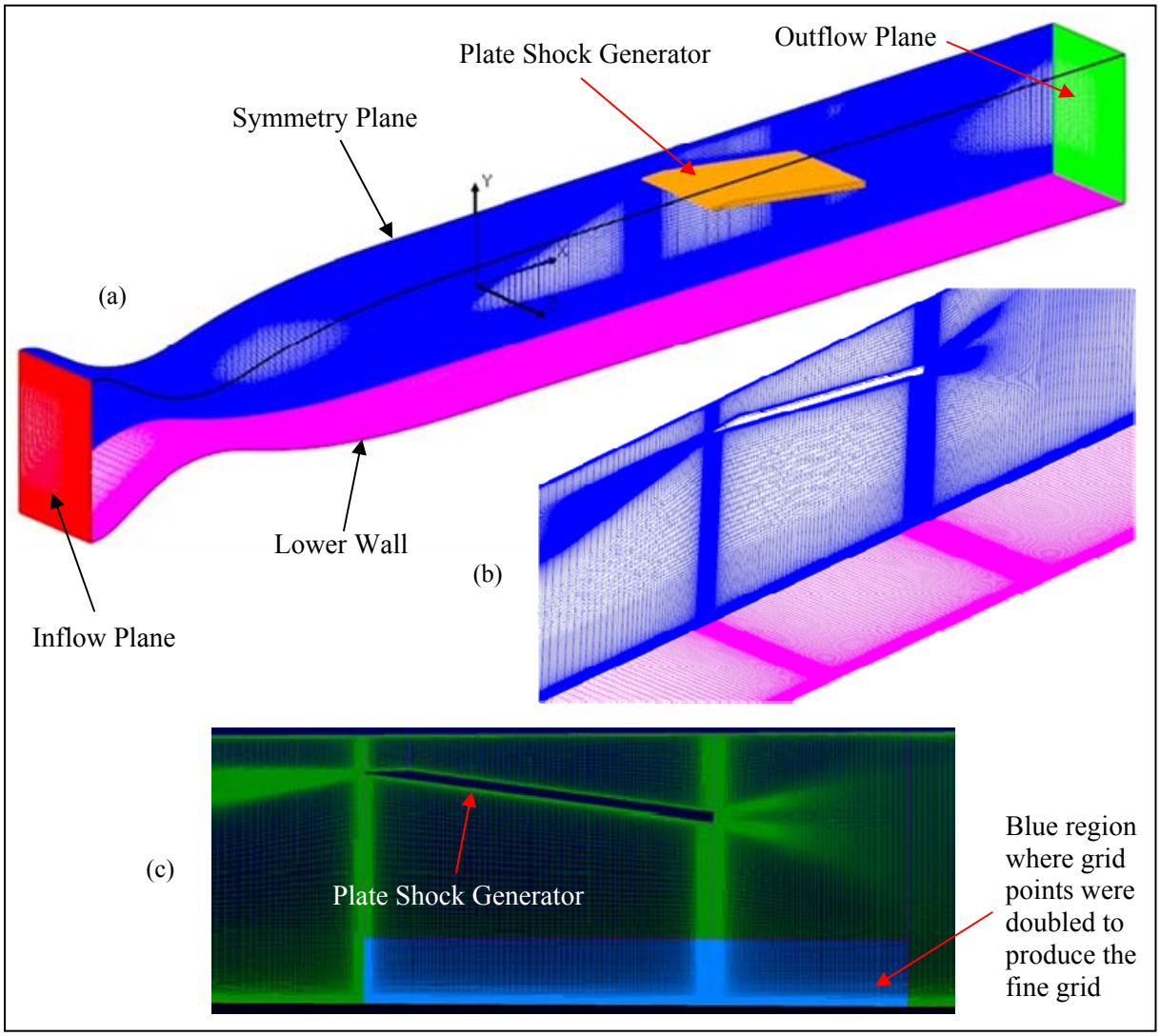

Figure 4. UFAST computational domain: (a) full length view, ~20.4M cells, (b) 3-D grid detail in test-section, and (c) 2-D grid detail in test-section. Grids generated in Pointwise v16.04R1. Note: only half the geometry was gridded.

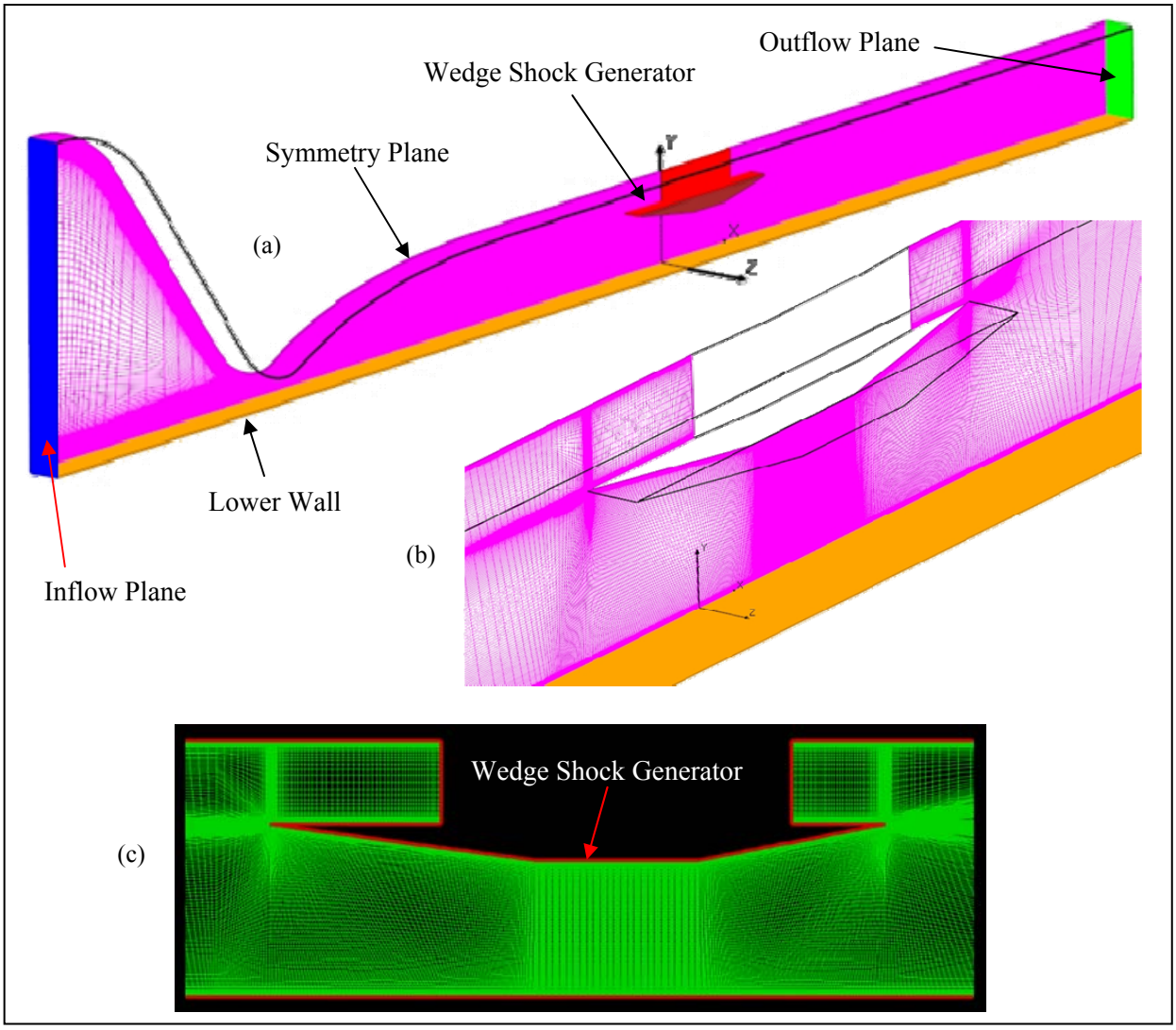

Figure 5. UMICH computational domain: (a) full length view, ~18M cells, (b) 3-D grid detail in test-section, and (c) 2-D grid detail in test-section. Grids generated in Gambit v2.4.6. Note: only half the geometry was gridded.

A grid independence study was conducted for the UFAST case using the SST turbulence model, where the baseline grid, termed the "medium" grid, consisted of 20.4M cells. The number of grid points in each x, y, z direction were halved (including the initial wall spacing) to produce the "coarse" grid consisting of 2.5M cells. The grid points were then doubled in each x, y, z direction (including the initial wall spacing), but only for a rectangular region enveloping the predicted SBLI zone (rendered in blue in figure 4c). This resulted in the "fine" grid that consisted of 47.4M cells.

Stagnation pressure and temperature conditions, as specified by the experiments, were imposed at the tunnel inlets (see table 2), while a centroidal extrapolation boundary condition was used at the outflow planes. The symmetry planes were modeled as inviscid walls (i.e., the "symmetry" boundary condition in CFD++). A viscous wall function boundary was used to model the strut

that supported the wedge-shaped shock generator in the UMICH tunnel; this maintains the same wall grid spacing on the symmetry plane and strut, thereby conserving grid size. All other walls were modeled as viscous, adiabatic walls with an initial y+ spacing of less than 1.

Table 2. Summary of simulation parameters.

PARAMETER	UFAST	UMICH
Shock Generator Angle	8.0º	7.75º, 10º, 12º
Mach #	2.25	2.75
Air Inlet Total Conditions	P_0=50.5 kPa, T_0=293 K	P_0=101 kPa, T_0=293 K
Outflow	Centroidal Extrapolation	
Wall Boundaries	Viscous, No-Slip, Adiabatic, except UMICH support strut	
Numerics	3-D, compressible, steady-state, RANS; finite volume method; point-implicit time integration w/ local CFL ramped from 1–40; multigrid W-cycle method; implicit temporal smoothing; second-order inviscid spatial discretization; upwind HLLC scheme; TVD continuous flux limiter	
Turbulence Models	(i) Menter's Shear Stress Transport (SST) (ii) Spalart-Allmaras (SA) (iii) Realizable k-ε (RKE) (iv) Cubic k-ε (CKE) (v) Goldberg's R_t Model (RT) (vi) Goldberg's k-ε-R (KER) (vii) Reynolds Stress Transport (RSM)	(i) Menter's Shear Stress Transport (SST) (ii) Spalart-Allmaras (SA) (iii) Realizable k-ε (RKE)
	Inlet Turbulence Intensity 0.1% Turbulence Length Scale 0.15175 m	Inlet Turbulence Intensity 1%; Turbulence Length Scale 0.08935 m
Computational Domain (Baseline Grids)	~20.4M Hexahedral Cells; ½ Geometry 136 Processors Pointwise v16.04R1	~18M Hexahedral Cells; ½ Geometry 120 Processors Gambit v2.4.6
	Δs_{wall}= 0.005 mm → y+ < 1	
Computing Hardware	"Harold" SGI Altix ICE 8200 10,752 2.8-GHz Intel Xeon Nehalem Cores 1344 Nodes, 24 GB RAM/ Node 4x DDR Infiniband Interconnect	"MJM" Linux Networx Advanced Tech Cluster 4400 3.0-GHz Intel Woodcrest Cores 1100 Nodes, 8 GB RAM/ Node 4x DDR Infiniband Interconnect

CFD++ v8.1.1 (*18*), a commercial fluid flow solver, was used to solve the 3-D, compressible, steady-state, RANS equations using a finite volume method. A point-implicit time integration scheme with local time-stepping, defined by the CFL (Courant-Friedrichs-Lewy) number, was used to advance the solutions towards steady-state. The CFL number was ramped typically from 1 to 40 over the first few hundred iterations, and remained at 40 until convergence. The multigrid W-cycle method with a maximum of four cycles and a maximum of 20 coarse grid levels was used to accelerate convergence. Implicit temporal smoothing was applied for increased stability. First-order spatial discretization was used for the first few hundred iterations, which then blended

over 100 iterations to second-order discretization. The inviscid flux function was an upwind scheme using a Harten-Lax-van Leer-Contact (HLLC) Riemann solver and Metacomp's multi-dimensional Total-Variation-Diminishing (TVD) continuous flux limiter.

Convergence was partially monitored by the reduction in the right-hand side residuals of the Navier-Stokes equations averaged over all cells at each iteration. The UFAST and UMICH cases typically demonstrated 8 and 4–5 orders of magnitude reduction in the residuals, respectively (see figure 6). Convergence for the UMICH case was more restricted, likely due to the prism elements in the test section grid. For the UFAST case, the exception was the seven-equation RSM turbulence model, which demonstrated only a 2–3 order of magnitude reduction in residuals. Also, it was ensured that the net mass and energy fluxes through the computational domain were driven to zero to satisfy mass and energy conservation laws.

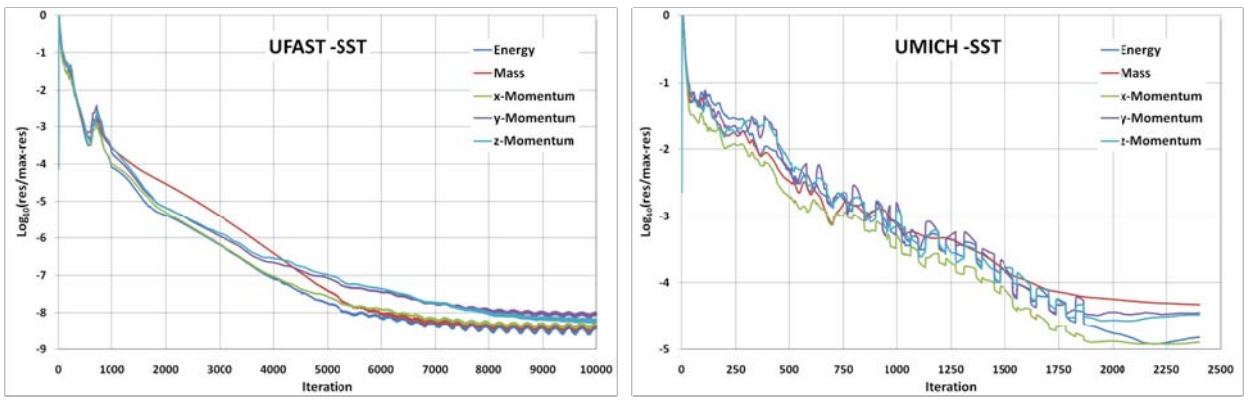

(a) (b)

Figure 6. Sample residual histories of the right-hand side equations: (a) UFAST – SST and (b) UMICH – SST.

The simulations were sensitive to the choice of turbulence model, as will be shown in section 3. Therefore, several turbulence models were investigated. Although some models are known to produce better results than others for internal flows, the authors tested almost all turbulence models available within CFD++ for the UFAST case, mainly for the purpose of completeness and future referencing.

For the UFAST case, the turbulence models tested were the:

1. Menter's Shear Stress Transport (SST) 2-equation model (16, 17, 20)
2. Spalart-Allmaras's (SA) 1-equation model (20, 21)
3. Realizable k-ε (RKE) 2-equation model (5, 20)
4. Cubic k-ε (CKE) non-linear, 2-equation model (11)
5. Goldberg's Rt (RT) 1-equation model (11)
6. Goldberg's k-ε-R (KER) 3-equation model (12)

7. Reynolds Stress Transport (RSM) 2nd moment closure, 7-equation model (2)

For the UMICH case, only the first three of the aforementioned models were used. (See table 2). The flows were assumed to be fully turbulent— i.e., no transition modeling was used.

The inlet turbulence intensity was chosen as 0.1% for the UFAST case (as determined by the experiment) and 1% for the UMICH case (as typically used for similar internal flows). The turbulent length scale was taken to be the square root of the cross-sectional area (as recommended by Metacomp (*18*)) of the inflow plane for the UFAST tunnel—i.e., 0.15175 m—and the test section for the UMICH tunnel—i.e., 0.08935 m. The laminar-to-turbulent Prandtl number ratio was chosen as default value 0.8. Metacomp's wall-bounded compressibility correction (*18*) was applied to realize diffusive mixing in the turbulent regions, which would otherwise be under-predicted in compressible flows.

3. Results

The following compares experimental and numerical data for the UFAST (section 3.1) and UMICH (section 3.2) wind tunnels. Plots include 3-D flowfield contours, numerical oil flow visualizations, and 2-D and 1-D velocity and perturbation velocity profiles for several turbulence models. Grid sensitivity is also demonstrated for the UFAST case. Except where turbulence models and grid densities are compared, the results are for the SST turbulence model using the "medium" grid, as this was the assumed baseline case. For the 2-D contour plots, the end-values on the legends are not necessarily the min/max values of the plotted flow variable; the legend end-values were, instead, altered for best visual rendering. All length scales are in meters, unless otherwise stated.

3.1 UFAST Wind Tunnel

Figure 7 provides a 3-D perspective of the flow in the tunnel test section, with Mach number contours on the symmetry plane and oil flow streamlines on the lower wall. Figure 8 compares experimental (*9*) and numerical oil flow streamlines on a plane 0.002 m above the lower wall. The adverse pressure gradient imposed by the incident shock induces a region of recirculation on the lower wall and thickens the boundary layer. The influence of the corner flow on the centerline core flow is very evident in both experiment and CFD, implying that the flow is highly three-dimensional. This was purported to be the result of shock waves thickening and possibly separating the corner flow boundary layers, which then pushes flow away from the walls towards the centerline, therefore altering the strength of the centerline SBLI (*3*). This effect will also be shown in the UMICH case in section 3.2. The coupling of the centerline and corner SBLIs, therefore, necessitates simultaneous accurate numerical prediction of both flows. However, due to the lack of experimental corner flow data, the CFD numerical modeling of the corner flow could not be verified; this, in turn, adds a source of uncertainty in predicting the centerline flow.

Note that the scales of the experimental and numerical plots in figure 8 are different. For the region z = –0.06–0.06 m, in the vicinity of x = 0.320 m, the centerline SBLI flow structure obtained via CFD (figure 8b) compares very well with that obtained via experiment (figure 8a).

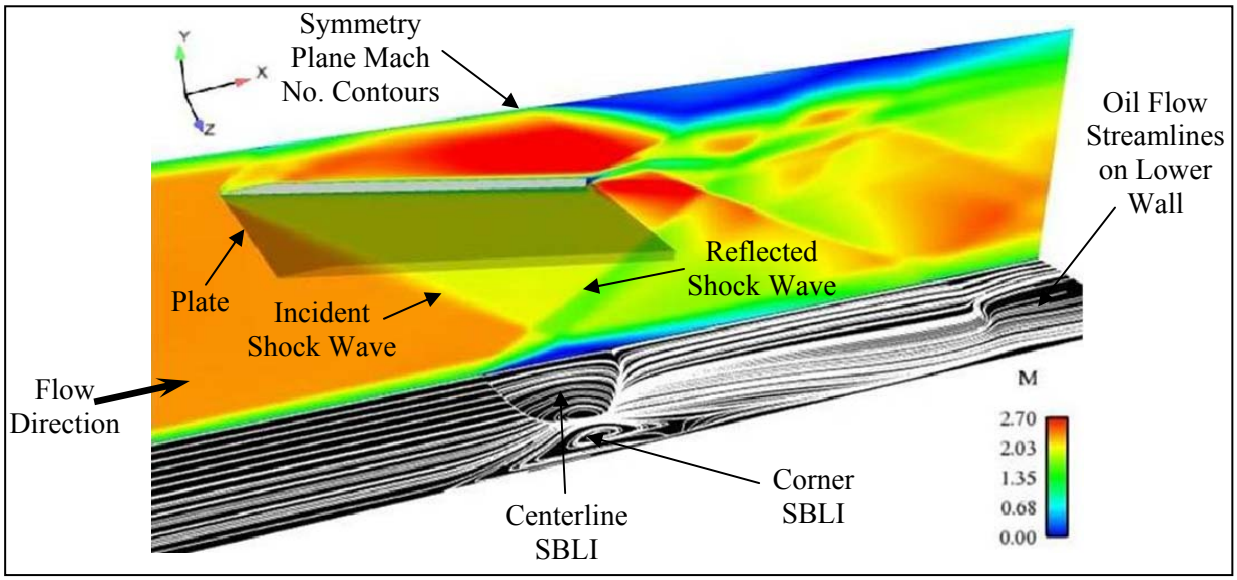

Figure 7. Three-dimensional rendering of UFAST numerical flowfield for SST turbulence model showing Mach number contours on the tunnel symmetry plane and oil flow streamlines on the tunnel lower wall.

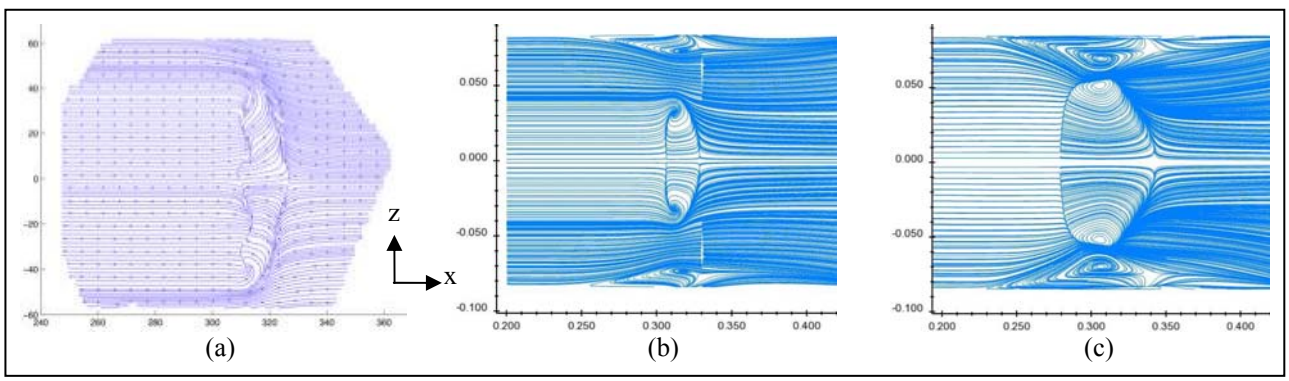

Figure 8. Transverse profile in the interaction zone showing centerline and corner SBLIs: (a) experimental SPIV data (*9*) on a plane 2 mm above the lower wall (scale units in mm), (b) CFD streamline data using SST turbulence model on a plane 2 mm above the lower wall (scale units in m), and (c) CFD streamline data using SST turbulence model on the lower wall (scale units in m).

Although seven turbulence models were simulated (see table 2), the contour plots of figures 9 and 10 depict only the "best" four, while the line plots of figures 11–13 depict all seven. The "best" turbulence models refer to those that compared best with experiment. In no particular order, these were the RSM, SA, Menter's SST and Goldberg's R_t models.

Figure 9 compares u-velocity and the numerical Schlieren (density gradient in the axial direction) between different turbulence models. The plots show the shock structure—a sequence

of oblique shock and expansion waves—induced by the plate in the wind tunnel test section. The different turbulence models produce slightly different characteristics, especially where the waves interact with the flow near the walls. The shock emanating from the leading edge of the plate impinges the boundary-layer on the bottom wall in the vicinity of x≈0.3–0.35 m (the SBLI zone). Typical aerodynamic SBLI characteristics consistent with that observed in the experiment can be identified (particularly from the Schlieren plots), such as the incident and reflected shocks, a λ-shock, an expansion fan, and increased boundary layer thickness due to adverse pressures.

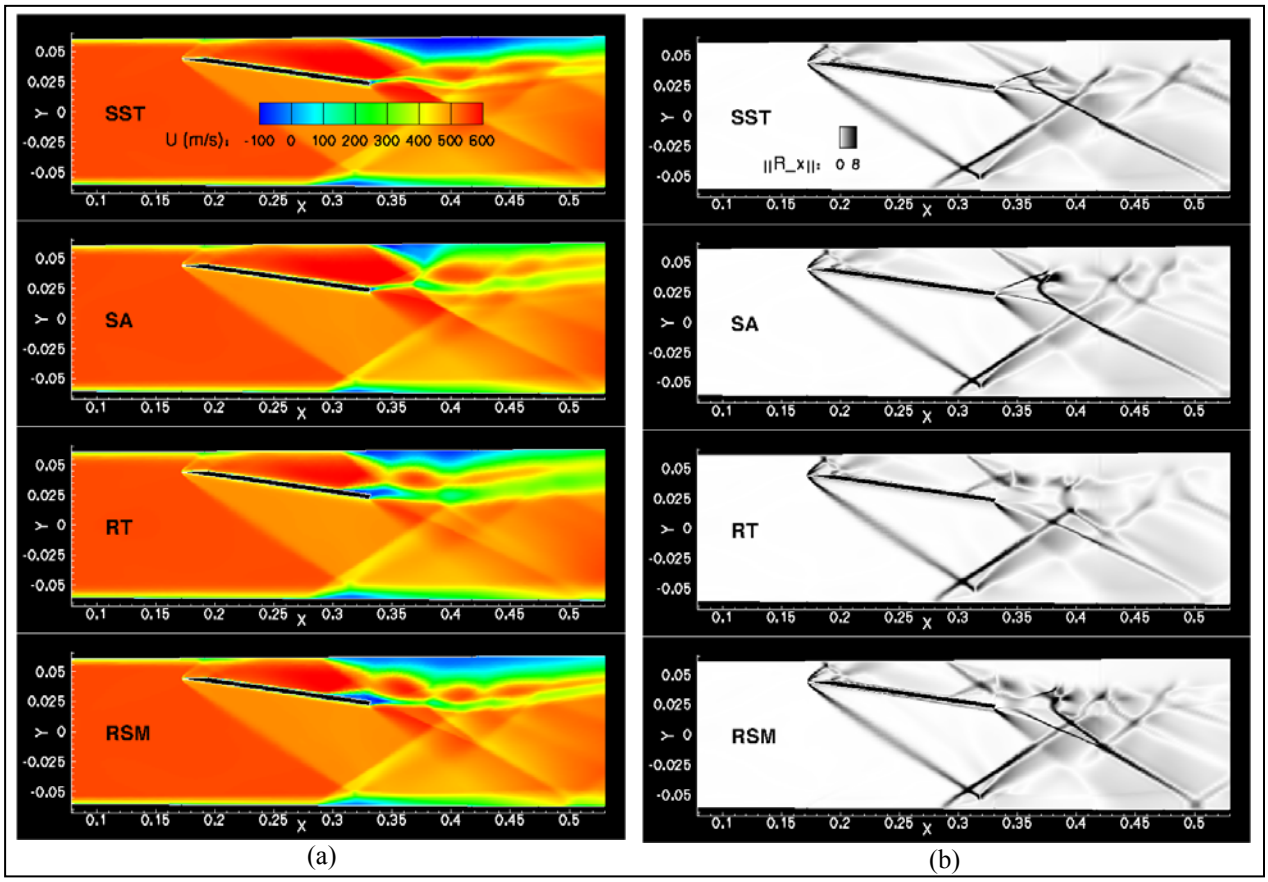

Figure 9. Turbulence model comparison on symmetry plane: (a) u-velocity and (b) numerical Schlieren.

Figure 10 compares u- and v-velocities in the SBLI zone between the experimental and numerical results. The SA and RSM models best capture the size and shape of the boundary layer in the interaction region, as well as the location of the interaction. The SST and RT models slightly over-predict the size of the interaction region; they also predict the interaction to occur slightly more upstream than that of the experiment.

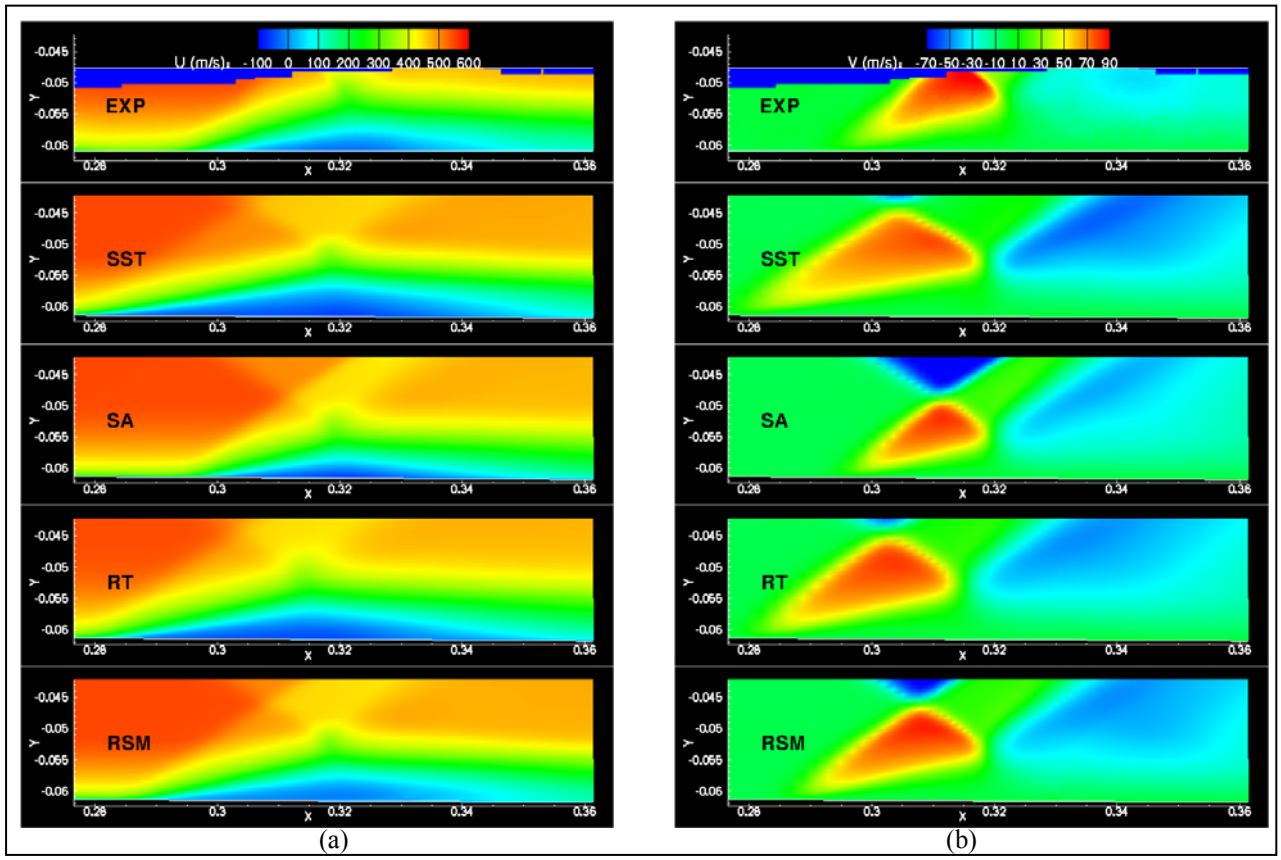

Figure 10. Experiment vs. CFD on symmetry plane in SBLI region: (a) u-velocity and (b) v-velocity.

Figures 11–13 compare 1-D axial profiles of u-velocity, v-velocity, and u′v′ Reynolds stress in the SBLI region. Upstream of the shock-induced pressure gradients, the velocity and perturbation velocity profiles are reasonably captured by all turbulence models. Progressing downstream, the disparity increases through the main interaction region, after which the agreement is again reasonable. There is increased sensitivity to turbulence modeling for the v-velocity and u′v′ Reynolds stress components. The observed discrepancies in figures 11–13 are partially due to the variation in the prediction of the SBLI location, as shown in figure 10. This error would be reflected as a translation of the numerical data along the x-axis.

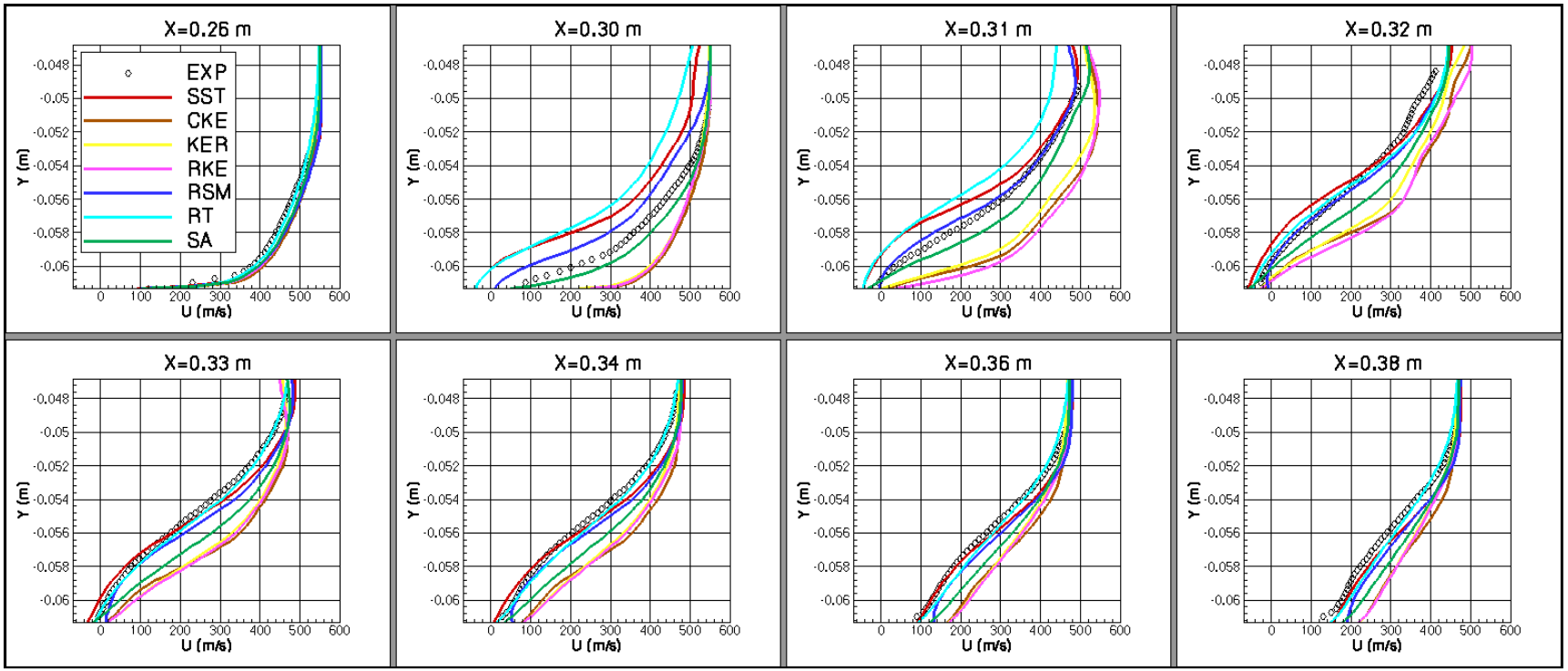

Figure 11. Turbulence model sensitivity: u-velocity axial profiles on the symmetry plane in the SBLI region.

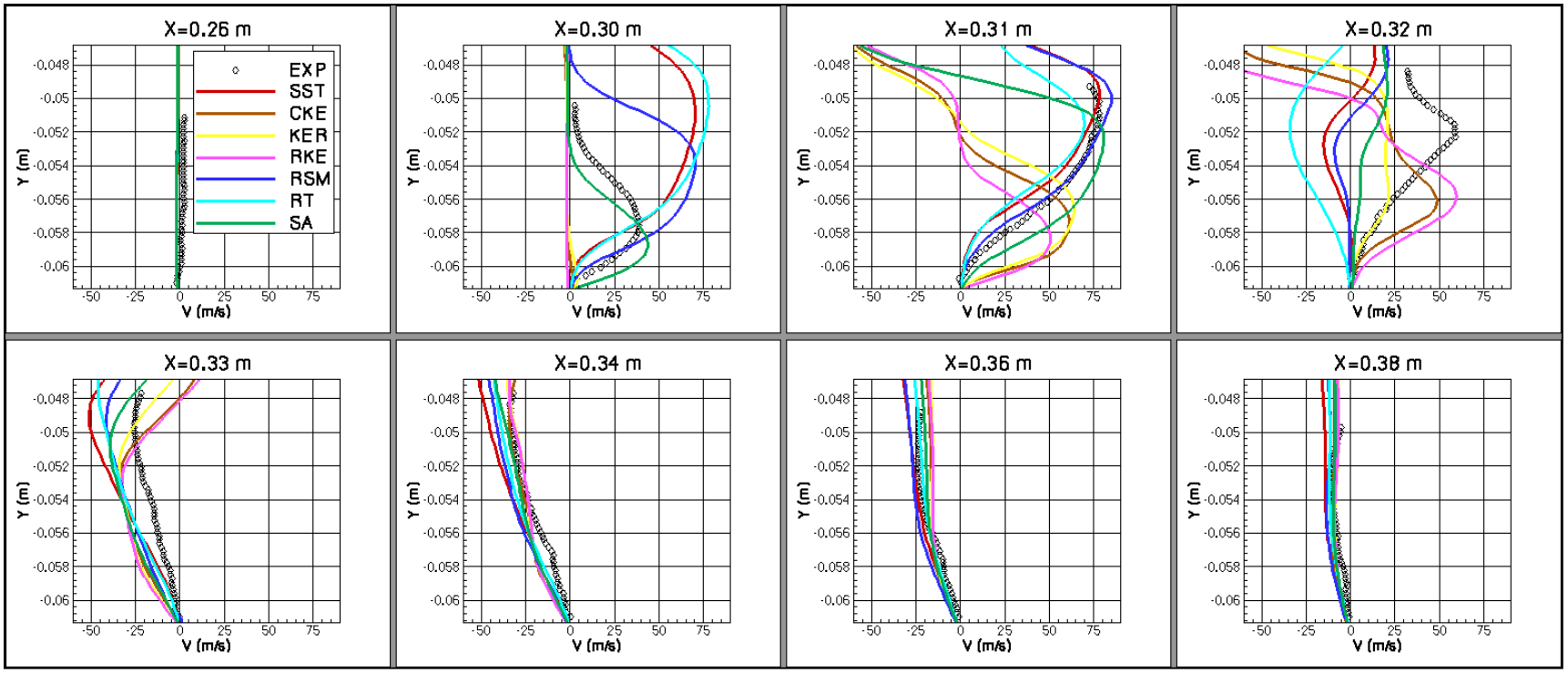

Figure 12. Turbulence model sensitivity: v-velocity axial profiles on the symmetry plane in the SBLI region.

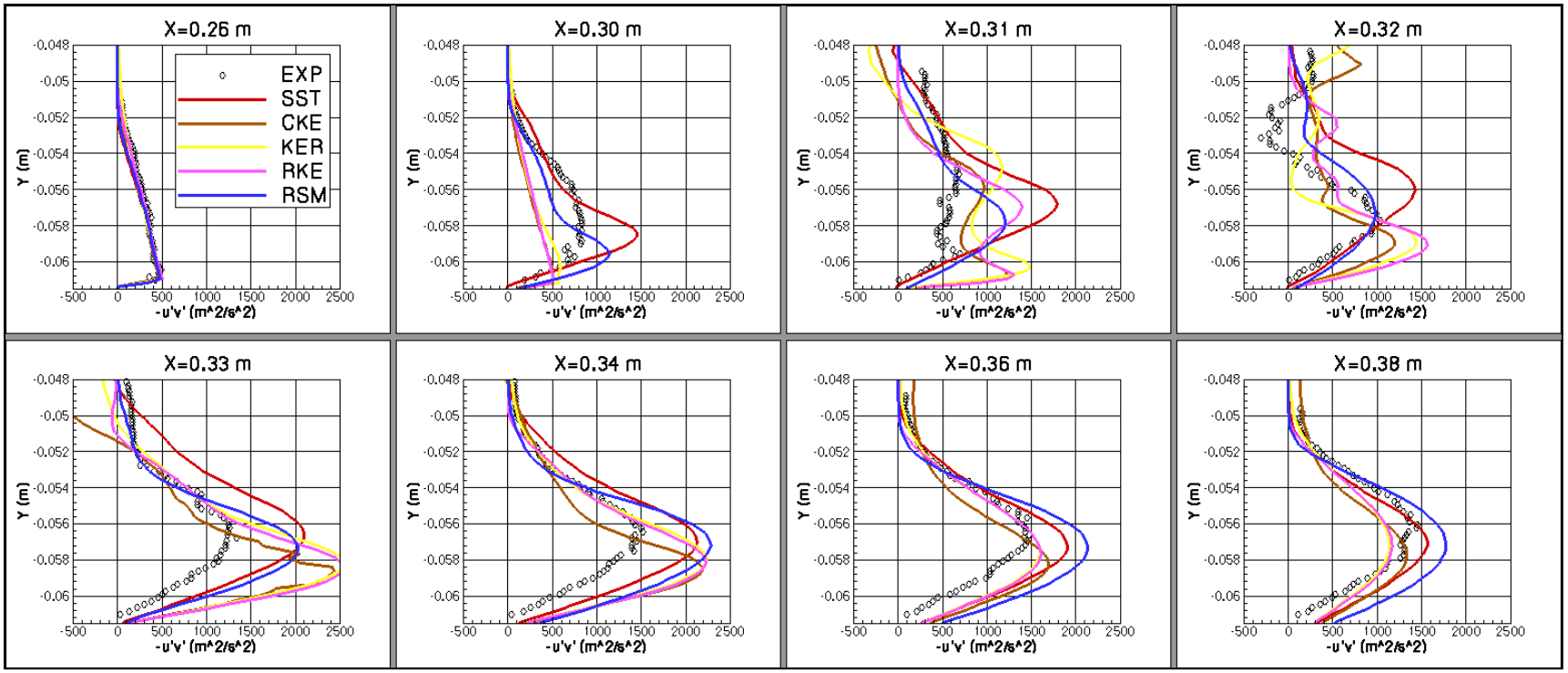

Figure 13. Turbulence model sensitivity: u′v′ axial profiles on the symmetry plane in the SBLI region.

Figures 14–17 show the results of a grid density study using the SST turbulence model (the aforementioned baseline model), where the coarse, medium, and fine grids consisted of 2.5, 20.4, and 47.4 million cells, respectively (as described in section 2). Figure 14 shows u- and v-velocity contour plots on the symmetry plane for each grid level. While the medium and fine grid results show qualitatively similar results, it is apparent that higher resolution of the shock-boundary layer interactions is obtained with each increase in grid density.

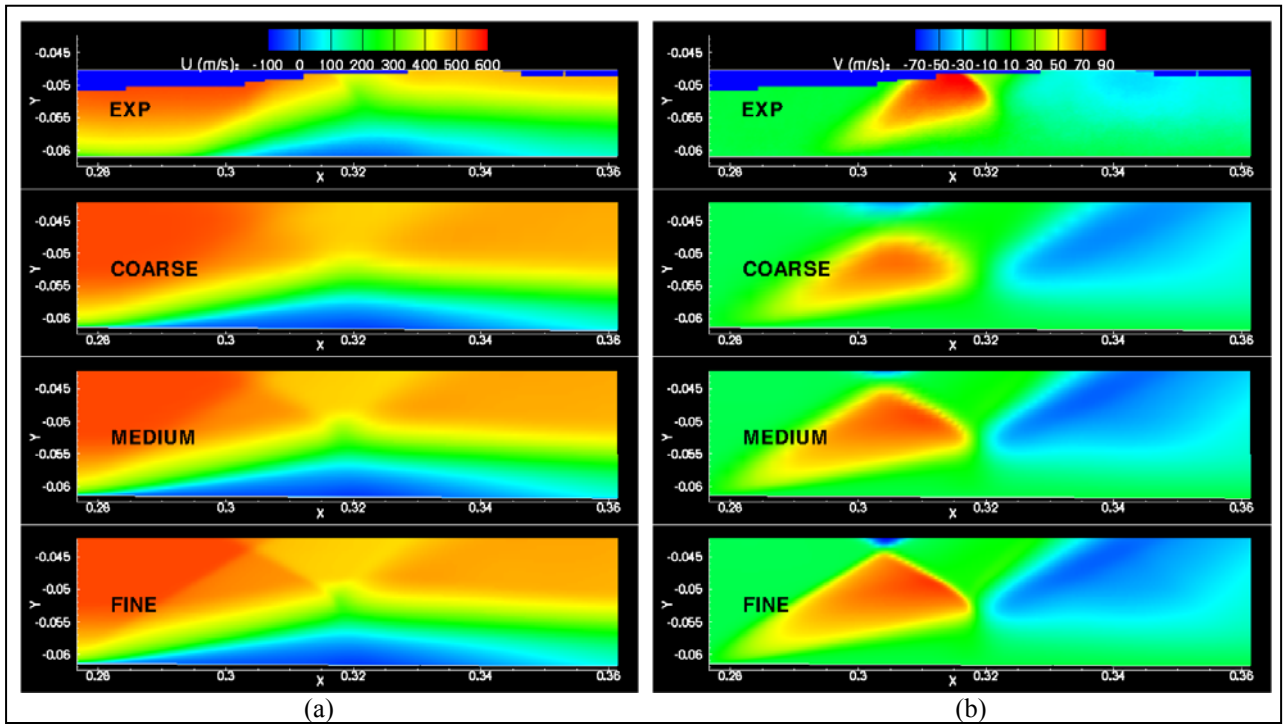

Figure 14. Grid sensitivity: (a) u-velocity and (b) v-velocity symmetry plane contours in SBLI region, SST model.

Figures 15–17 compare 1-D axial profiles of u-velocity, v-velocity, and u′v′ Reynolds stress on the symmetry plane for the three grid levels. For the u-velocity variable, the medium and fine grid plots overlay each other, while for the v-velocity and u′v′ Reynolds stress, the medium and fine grids very closely match. This indicates that grid independence was achieved with the medium grid and was, therefore, deemed sufficient for all other UFAST computations.

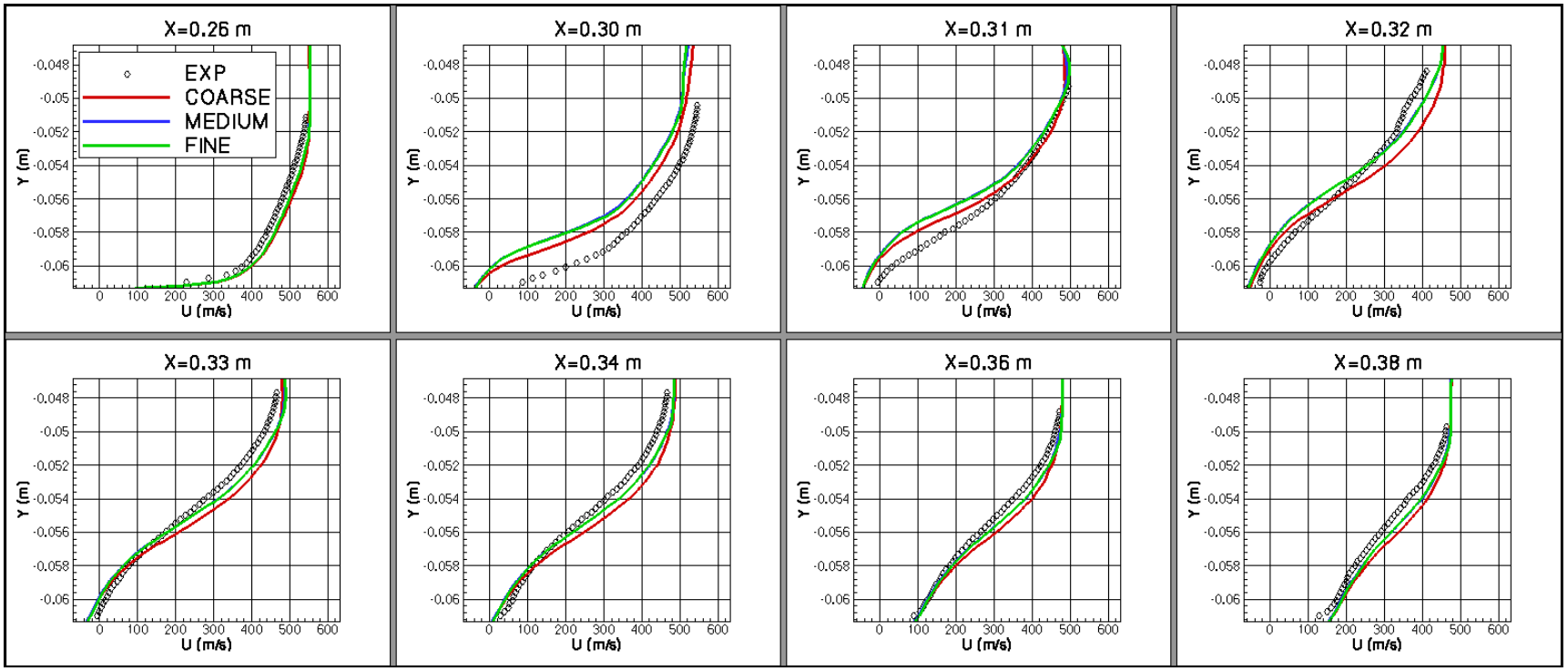

Figure 15. Grid sensitivity: u-velocity axial profiles on the symmetry plane in the SBLI region, SST model.

Note that the fine grid results (green) overlay that of the medium grid (blue).

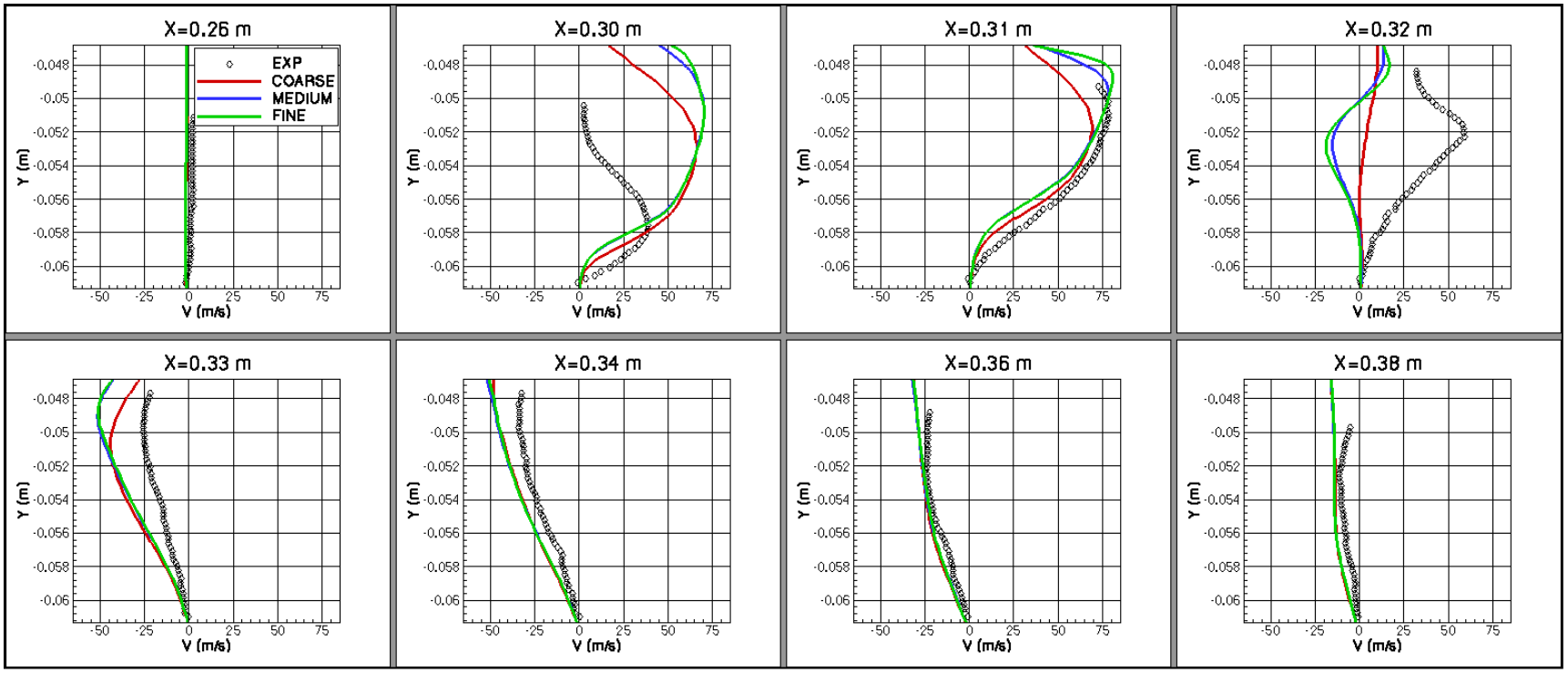

Figure 16. Grid sensitivity: v-velocity axial profiles on the symmetry plane in the SBLI region, SST model.

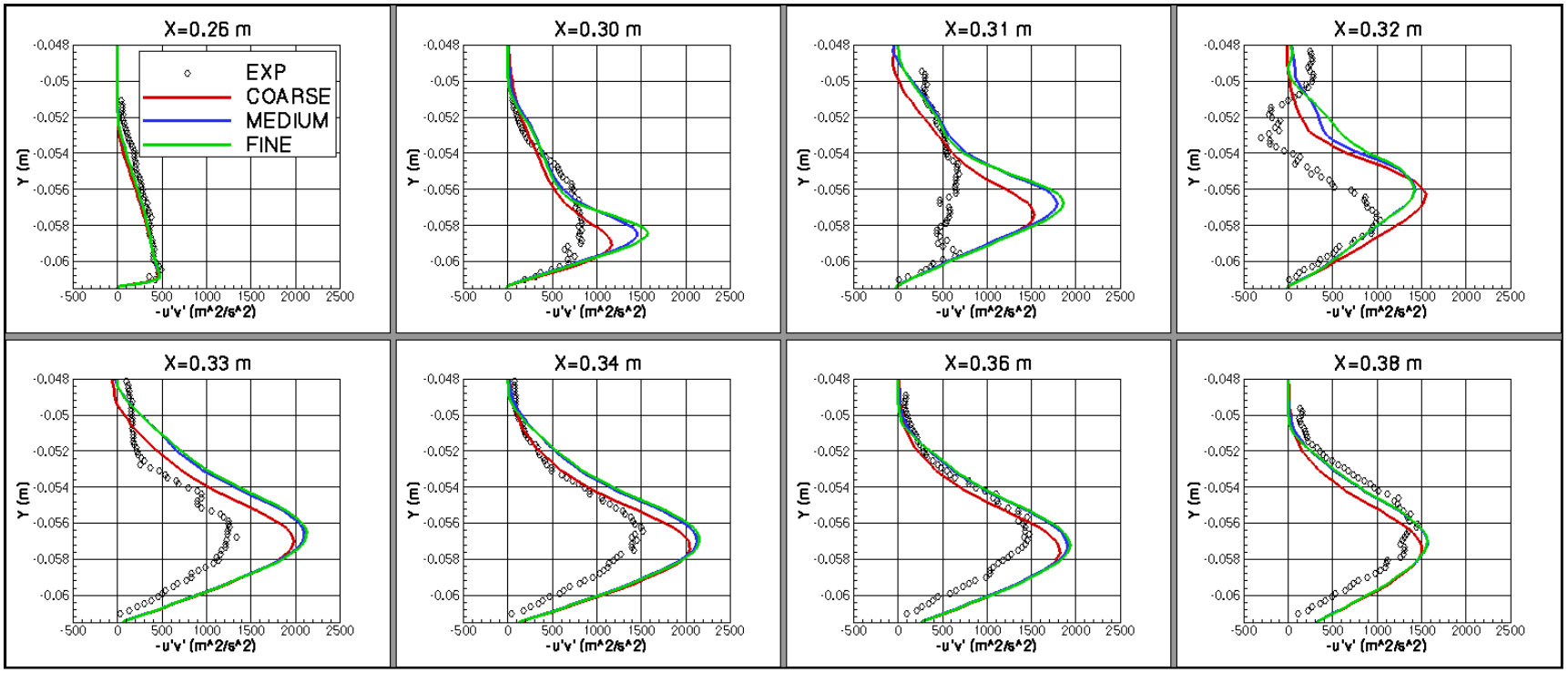

Figure 17. Grid sensitivity: u′v′ axial profiles on the symmetry plane in the SBLI region, SST model.

For a symmetric duct with a uniform symmetric inflow (as is the case here), it is expected that the flowfield downstream of the inflow would also be symmetric. This would normally be true for both experimental and numerical flowpaths. However, it was briefly discussed at the SBLI Workshop that flow asymmetries were observed in some of the UFAST experiments; these experiments may or may not have included the one simulated in this study, but were performed using the same wind tunnel. It was also suggested that this may also occur in numerical simulations and that the results may be physically real. Recall that all simulation results presented so far were for half of the UFAST flowpath, since a symmetric flowfield was assumed. To explore possible flow asymmetries, the baseline medium level "half" grid was mirrored to produce the "full" grid, and the simulation was re-run (using the SST turbulence model). Mirroring the grid eliminates the possibility of an asymmetric flowfield developing because of an asymmetric grid. These results also provide some qualitative insight into the spanwise flowfield profiles.

Figure 18 compares pressure contours on the lower wall (where the SBLI occurs) for the full grid and half grid. The contour plot for the half grid is mirrored for better visual comparison. Figures 19–21 compare pressure, skin friction, and u-velocity at three axial locations—x=0.20, 0.32, and 0.40 m. The pressure and skin friction line data were extracted from the lower wall across the span (z-direction) of the tunnel. To verify symmetry using the line plots, the +z and –z data were superimposed on each other, i.e., the -z data was mirrored about the z=0 axis. All results indicate that, from a numerical standpoint, the flowfield using the full grid is very symmetric and produces the same results as the half grid. It is possible that asymmetries observed in the experiment may be due to spanwise asymmetries in the tunnel hardware and/or inflow conditions.

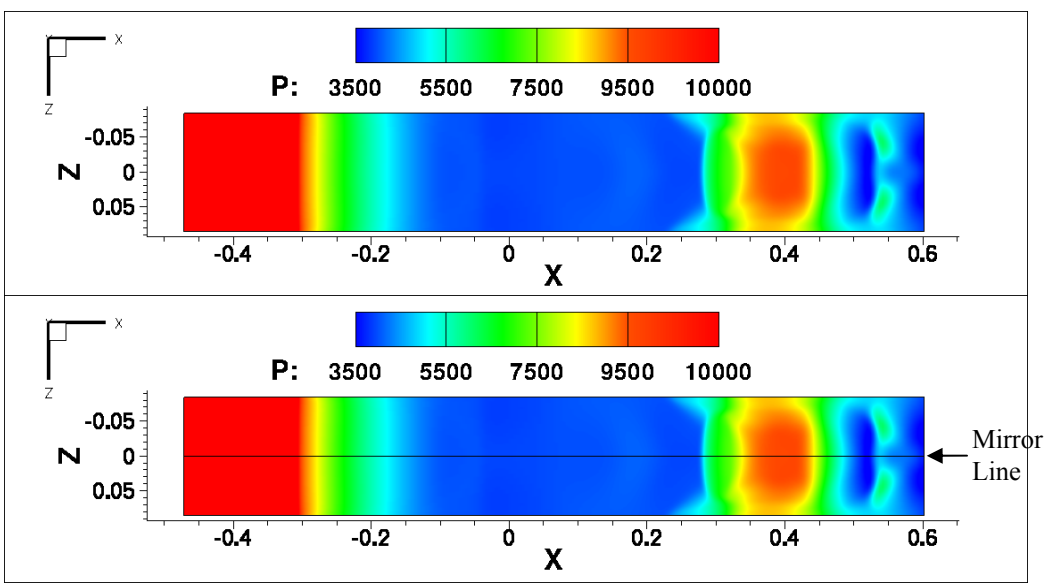

Figure 18. Pressure contours on the lower wall for the (a) full grid and (b) mirrored half grid, SST model.

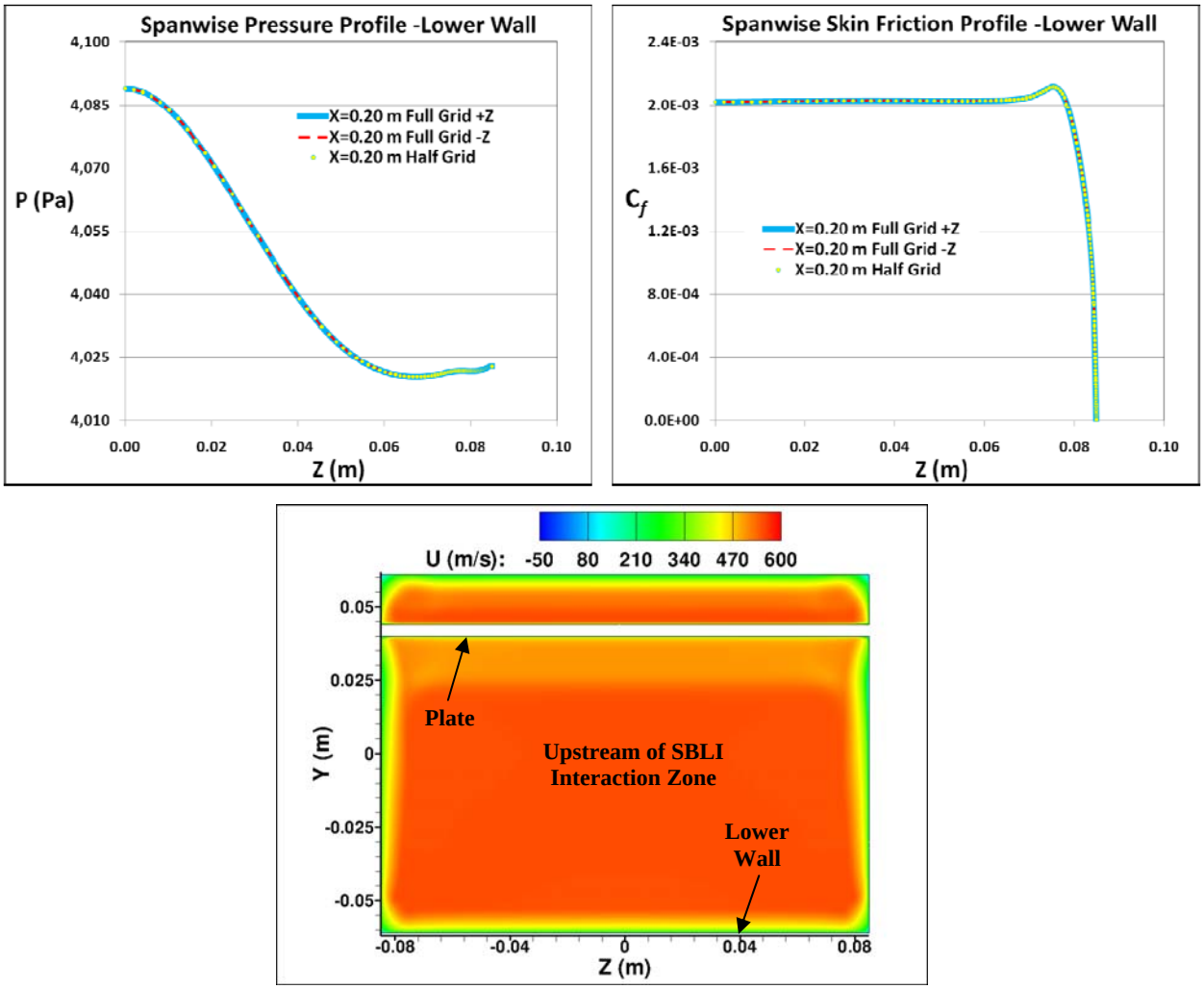

Figure 19. Spanwise profiles of pressure, skin friction and velocity using full grid, X=0.20 m, SST model.

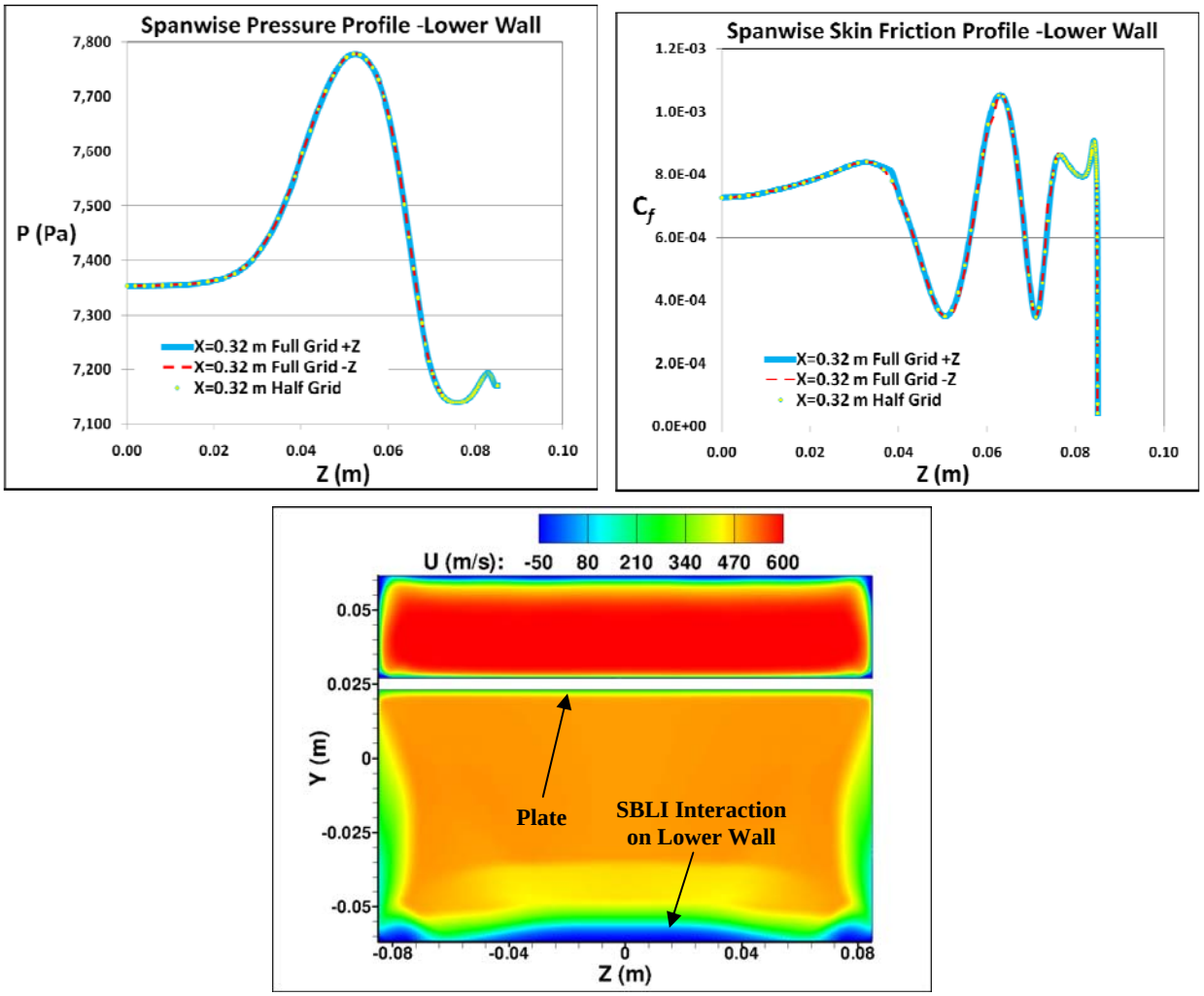

Figure 20. Spanwise profiles of pressure, skin friction and velocity using full grid, X=0.32 m, SST model.

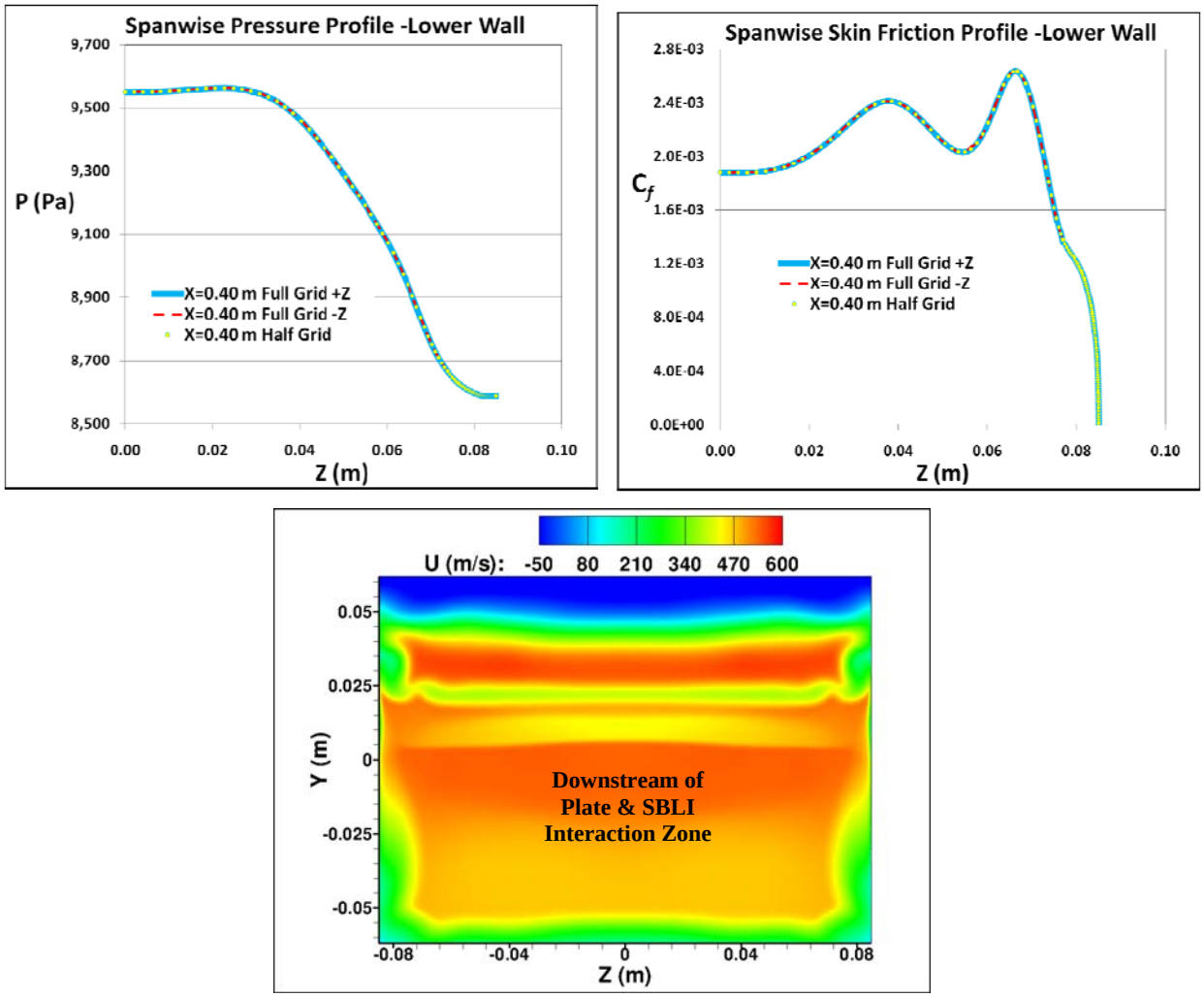

Figure 21. Spanwise profiles of pressure, skin friction and velocity using full grid, X=0.40 m, SST model.

3.2 UMICH Wind Tunnel

As described in section 1—Introduction, the results presented here were those presented at the AIAA SBLI Workshop. No further simulations, other than additional post-processing of the data, were completed after the Workshop. The UMICH results include three shock-generator wedge angles, viz, 7.75°, 10°, and 12° (test cases 2, 3, and 4). Results are first presented for the 7.75° case, which includes comparisons of three turbulence models, viz, SST, SA, and RKE. The effect of wedge angle on the flowfield is then compared via numerical contour plots in the tunnel section. All experimental and numerical test conditions and run parameters were the same for each wedge angle case. All UMICH simulations were conducted using a single grid level.

Figure 22 provides a 3-D perspective of the flow in the tunnel test section, with Mach number contours on the symmetry plane and oil flow streamlines on the lower wall. Although this result is for the SST turbulence model with wedge angle 7.75°, it represents the general flowfield of all the UMICH cases. The adverse pressure gradient imposed by the incident shock induces a region

of recirculation on the lower wall and thickens the boundary layer. Similar to the UFAST case, the influence of the corner flow on the centerline core flow is very evident in the CFD results, implying that the flow is highly three-dimensional. This flow structure is due to the coupling of the corner and centerline SBLIs, as described in the UFAST case (section 3.1). As previously stated, lack of corner flow data lends to a source of uncertainty in numerically predicting the centerline flow.

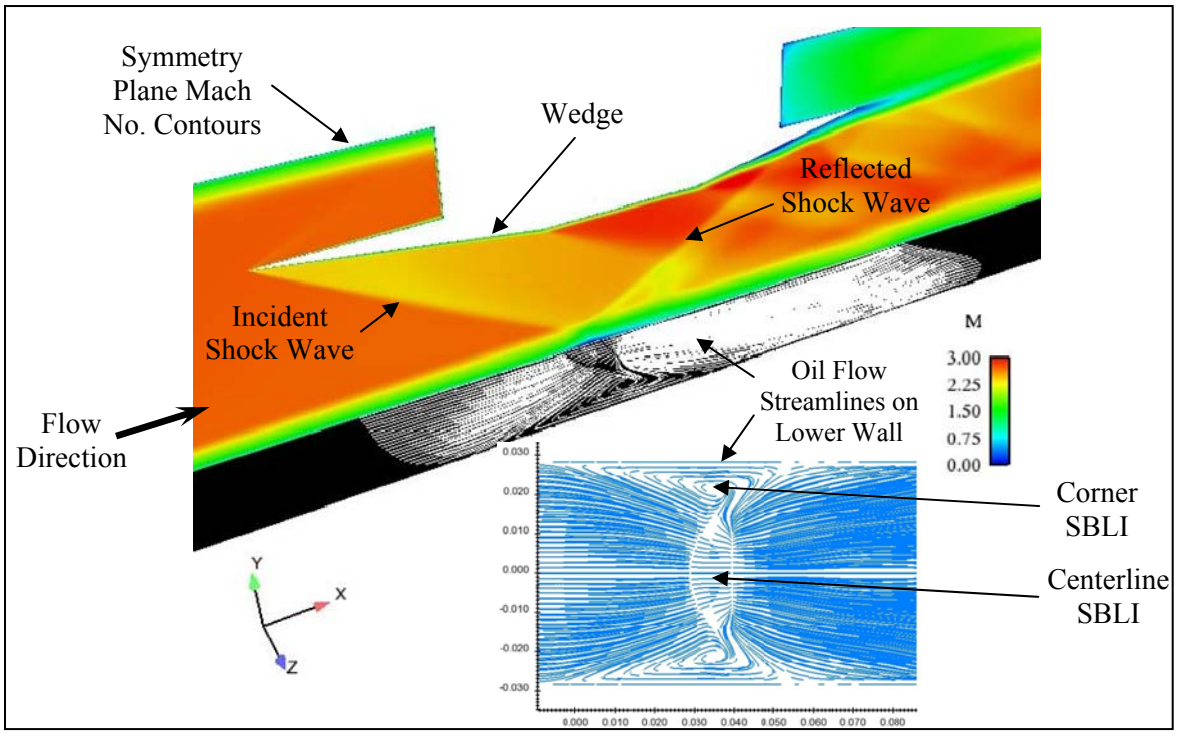

Figure 22. Three-dimensional rendering of UMICH numerical flowfield showing Mach number contours on the tunnel symmetry plane and oil flow streamlines on the tunnel lower wall, SST model, 7.75° case.

Figure 23 compares u-velocity and the numerical Schlieren (density gradient in the axial direction) between different turbulence models for the 7.75° case. The plots show the shock structure, a sequence of oblique shock and expansion waves induced by the wedge-shaped shock generator in the wind tunnel test section. The different turbulence models produce slightly different characteristics, especially where the waves interact with the flow near the walls. The choice of turbulence model seems to have a more subtle effect on the overall flowfield than for the UFAST case, possibly because of a higher inflow Mach number and resulting stronger shock waves in the test section. The shock emanating from the leading edge of the plate impinges the boundary-layer on the bottom wall in the vicinity of x≈0.03–0.04 m (the SBLI zone). Aerodynamic flow structures similar to that of the UFAST case can be identified in the SBLI region.

Factors such as grid resolution and corner flow influence may be partially responsible for the discrepancies. Future studies may include a grid density study, additional turbulence models, and data comparison for other flow variables (such as the Reynolds stress).

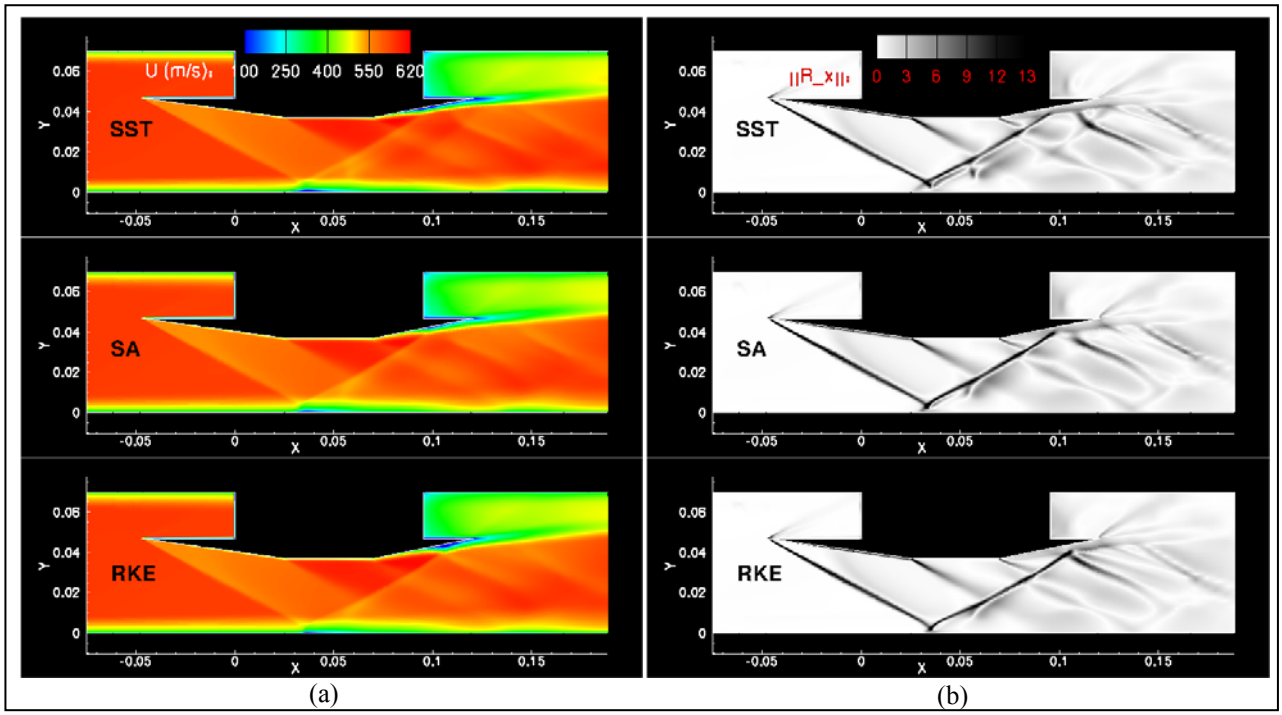

Figure 23. Turbulence model comparison on symmetry plane: (a) u-velocity and (b) numerical Schlieren, 7.75° case.

Figure 24 compares u- and v-velocity contours in the SBLI zone between the experimental and numerical results for the 7.75° case. Although the extent of the interaction is under-predicted by the SST model, this model best captures the size and shape of the recirculation region in the boundary layer, as well as the location of the interaction. The SA and RKE models show smaller interaction regions that occur slightly more downstream (~0.002–0.003 m) than in the experiment.

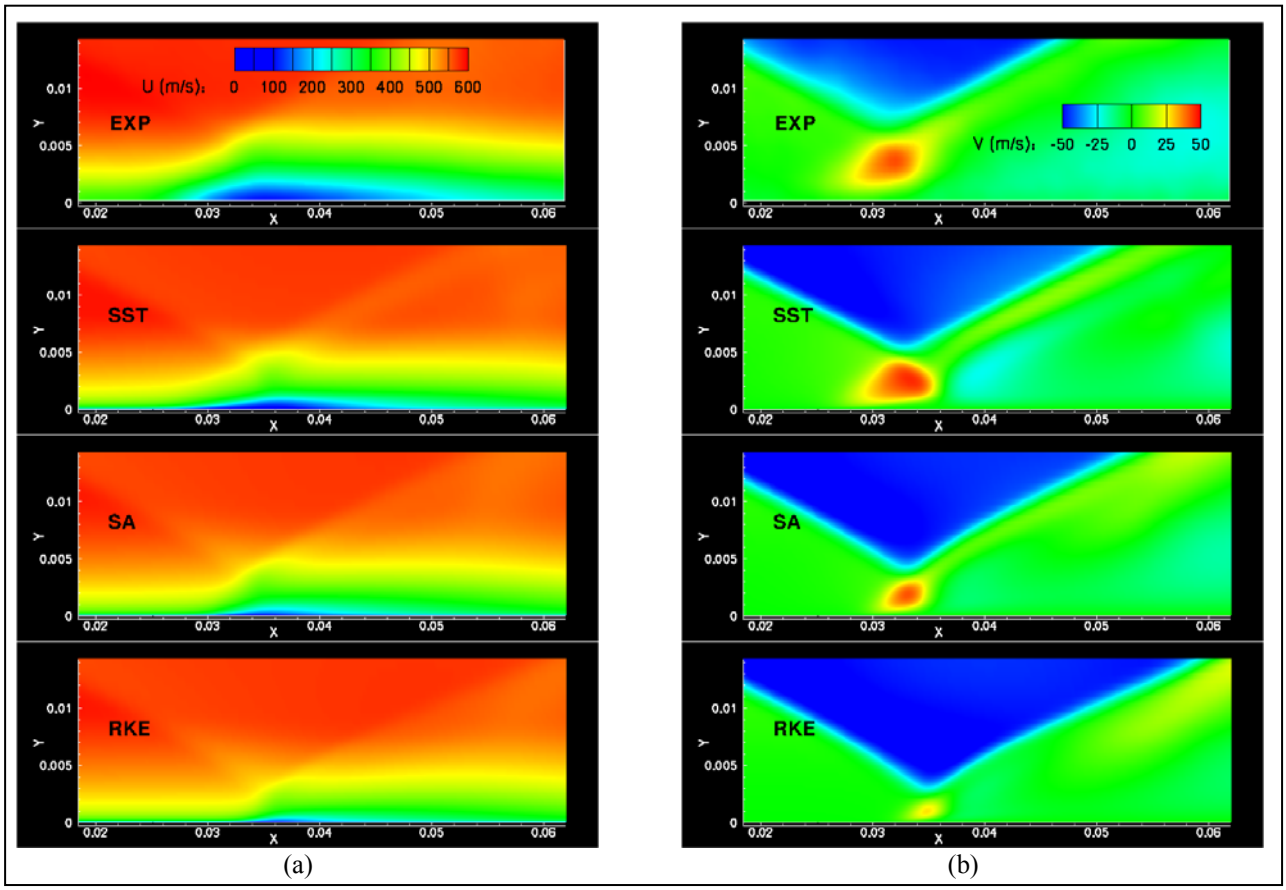

Figure 24. Experiment vs. CFD on symmetry plane in SBLI region: (a) u-velocity and (b) v-velocity.

Figures 25 and 26 compare 1-D axial profiles of u- and v-velocity in the SBLI zone between the experimental and numerical results for the 7.75° case. The CFD u-velocity profiles match very well with that of the experiment for the SST and SA models, and fairly so for the RKE model. Like the UFAST case, the v-velocity profiles are more sensitive to turbulence modeling. There is a larger discrepancy between the numerical and experimental results for this variable. Again, the SST and SA models are favored since the RKE model provides the worst comparison with experiment. However, improved prediction of the v-velocity variable is needed.

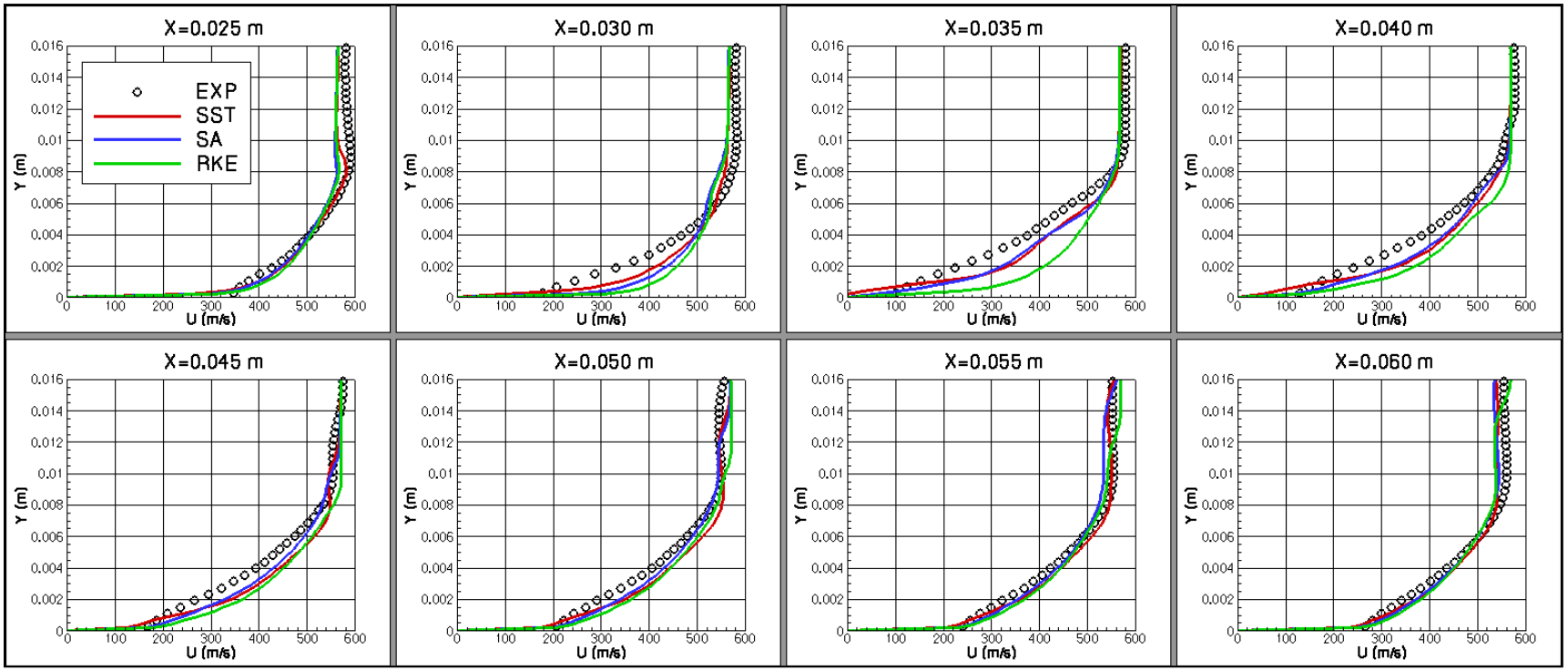

Figure 25. Turbulence model sensitivity: u-velocity axial profiles on the symmetry plane in the SBLI region.

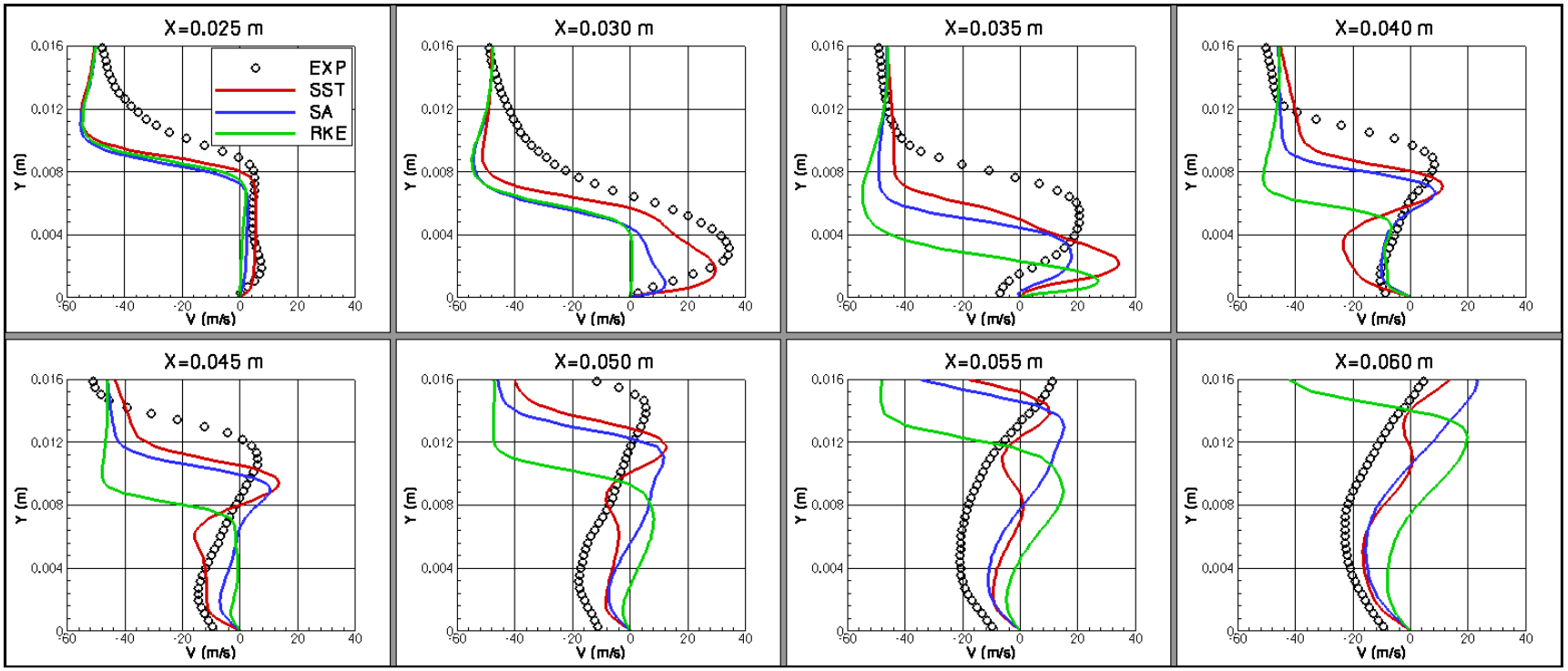

Figure 26. Turbulence model sensitivity: v-velocity axial profiles on the symmetry plane in the SBLI region.

The following results compare the effect of the shock-generator wedge angle on the test section flowfield and the SBLI zone. These wedge angles include 7.75°, 10°, and 12°, which comprise test cases 2, 3, and 4 (see section 1). Figure 27 shows Mach number contours and the numerical Schlieren on the test section symmetry plane for each wedge angle. While the shock structures are similar, it is observed that a larger wedge angle induces a leading edge shock that is stronger and has a larger angle of incidence (angle between the shock plane and the tunnel axis). The Mach number contours of figure 28 shows that this incurs stronger adverse pressure gradients at the lower wall, producing the observed larger recirculation region.

A larger incident shock angle, induced by a larger wedge angle, is expected to move the SBLI location further upstream. However, note that the leading edge of the wedge is further downstream for the larger wedge angles (figure 27). The net effect is to, instead, move the SBLI location further downstream (figure 28).

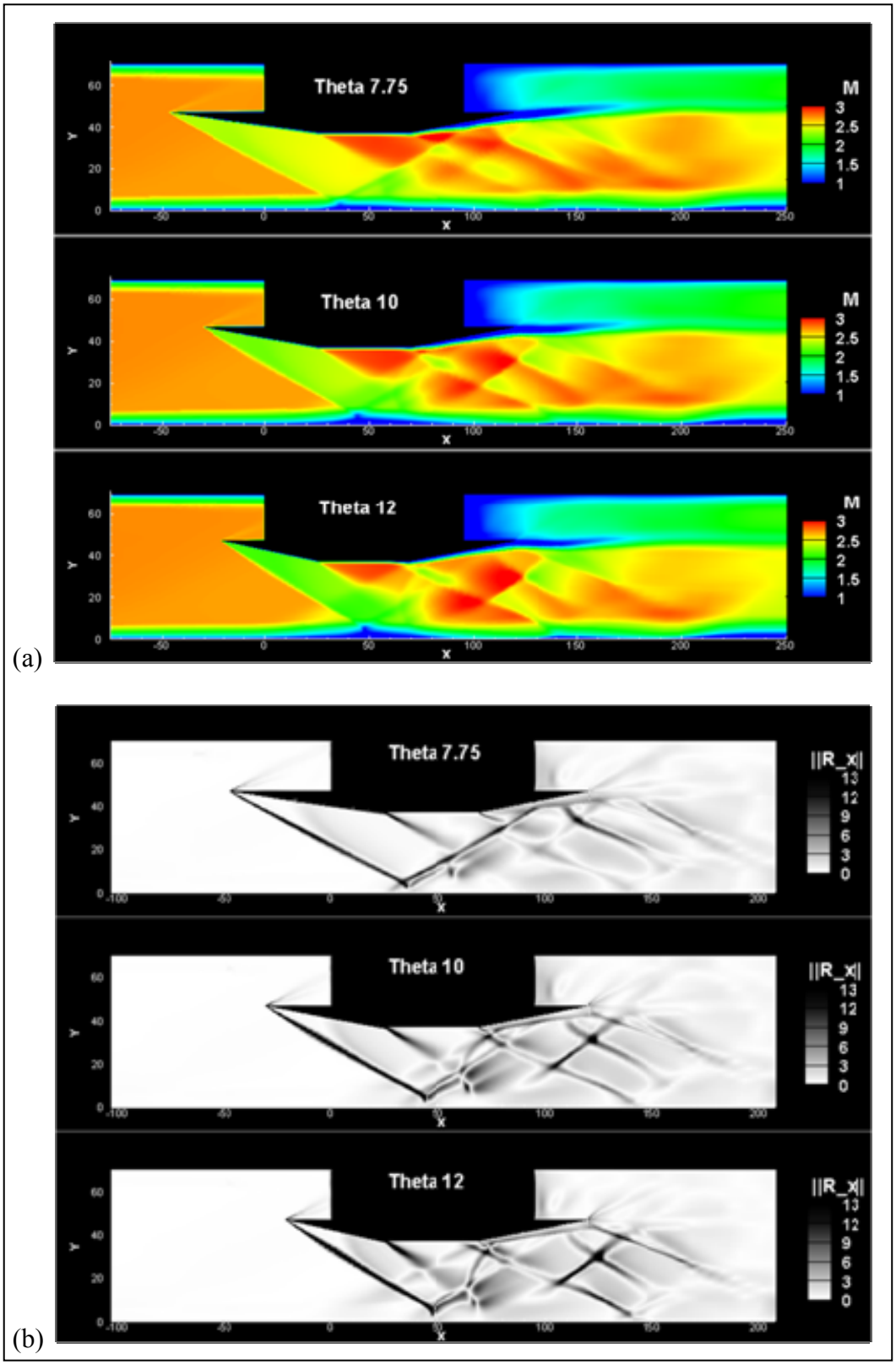

Figure 27. Effect of shock-generator wedge angle on the test section flowfield – symmetry plane numerical contours of: (a) Mach number and (b) numerical Schlieren. Plots are in mm.

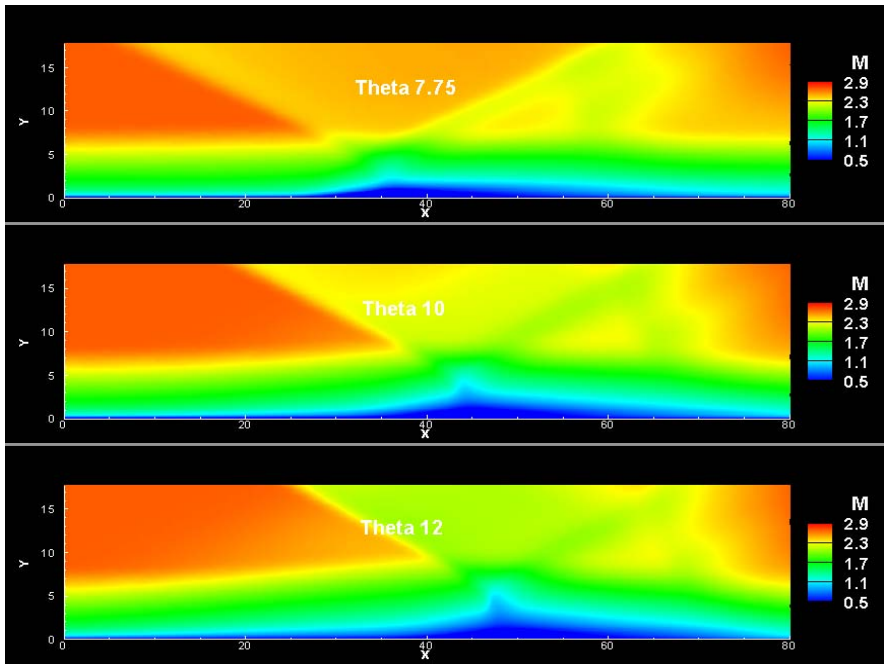

Figure 28. Effect of shock-generator wedge angle on the SBLI: Mach number numerical contours on the symmetry plane near the lower wall. Plots are in mm.

4. Summary and Conclusions

Shock-boundary layer interaction has been numerically simulated using steady-state RANS methods in two wind tunnel facilities, viz, UFAST and UMICH. Typical flow characteristics were identified, such as the recirculation region, incident, reflected, and λ shocks, and increase in boundary layer thickness. The accuracy of the numerical predictions in the shock-boundary layer interaction region was good in some cases and poor in others, and highly dependent on turbulence model chosen. The prediction of the v-velocity component and Reynolds stresses were more sensitive than the prediction of the u-velocity component. Observed inaccuracies may be the result of one or more factors. Inflow turbulence conditions may not have been adequately modeled due to lack of data from the experiments. Also, inadequacies in the turbulence model formulation, such as their inherent empiricisms, can lead to errors that are difficult to characterize. A lack of experimental corner flow data, which was shown to be coupled to the centerline flow, also adds a measure of uncertainty in the numerical results. Future studies will attempt to address some of these issues.

A suite of RANS turbulence models was studied, particularly for the UFAST case. Based on these studies, it appears that four of these models are best for internal flows where shock-boundary layer interaction phenomena occur. These were the Menter's SST, the SA, the Goldberg RT, and the RSM models. However, the choice of turbulence model is contingent upon

the type of problem being solved, as well as time/computing constraints. For the instance, the SST model is a two-equation model that takes about twice as long to produce a converged solution as compared to the one-equation SA or RT models. Therefore, the SA and RT models may be more desirable where rapid solutions are needed, as is the case in industrial applications. The RSM model—because it is a seven-equation model and requires very fine grid spacing near viscous walls, resulting in larger grid sizes—demands far more computational resources, and may also be less stable. Hybrid RANS/LES will be used in a future study, not only for comparison purposes, but to also resolve possible unsteady effects, such as resonance of the reflected shock wave from the boundary layer, as observed in the UFAST experiment.

Given the large grid sizes required to quantitatively resolve the flow in the SBLI region, an adaptive gridding technique may offer improved accuracy, while minimizing grid sizes. In such a case, grid points would be concentrated in high gradient regions via an automated procedure.

The results of this study conform to the general conclusions derived from the AIAA SBLI Workshop (*3, 6, 13*). Error margins observed in the numerical solutions submitted by all participants indicated that, for a single simulation methodology, good prediction of one flow variable does not guarantee good prediction of another. Therefore, no discernable trends could be elicited from the collective results of the participants. However, it was agreed that the dominant factors in the RANS prediction of SBLI were the choice of turbulence model and grid density.

5. References

1. Bardin, J. E.; Coakley, T. J. *Three-dimensional Navier-stokes Simulations with Two-equation Turbulence Models of Intersecting Shock-Waves/Turbulent Boundary Layer at Mach 8.3*; AIAA 94-1905; June 1994.

2. Batten, P.; Craft, T. J.; Leschziner, M. A.; Loyau, H. Reynolds-stress-transport Modeling for Compressible Aerodynamics Applications. *AIAA Journal* **July 1999**, *37* (7), 785–797.

3. Benek, J. A. *Lessons Learned from the 2010 AIAA Shock Boundary Layer Interaction Prediction Workshop*; AIAA 2010-4825; June/July 2010.

4. Benek, J. A. *Overview of the 2010 AIAA Shock Boundary Layer Interaction Prediction Workshop*; AIAA 2010-4821; July 2010.

5. Chien, K-Y. Predictions of Channel and Boundary Layer Flows with a Low-Reynolds-Number Turbulence Model. *AIAA Journal* **1982**, *20* (1), 33–38.

6. DeBonis, J. R.; Oberkampf, W. L.; Wolf, R. T.; Orkwis, P. D.; Turner, M. G.; Babinsky, H. *Assessment of CFD Models for Shock Boundary-Layer Interaction*; AIAA 2010-4823; June/July 2010.

7. Dolling, D. S. Fifty Years of Shock-Wave/Boundary-Layer Interaction Research: What Next? *AIAA Journal* **August 2001**, *39* (8), 1517–1531.

8. Dolling, D. S.; Murphy, M. T. Unsteadiness of the Separation Shock Wave Structure in a Supersonic Compression Ramp Flowfield. *AIAA Journal* **December 1983**, *21* (12), 1628–1634.

9. Dupont, P.; Debieve, J. F.; Dussauge, J. P.; Piponniau, S.; Souverein, L. J. Final Report on the Measurements of Shock Reflection at M=2.25. Groupe Supersonique, Laboratoire IUSTI, Ecole Polytechnique Universitaire de Marseille, Deliverable No 3.3.5, May 12, 2009.

10. Dupont, P.; Piponniau, S.; Sidorenko, A.; Debiève, J. F. Investigation by Particle Image Velocimetry Measurements of Oblique Shock Reflection with Separation. *AIAA Journal* **June 2008**, *46* (6).

11. Goldberg, U.; Batten, P.; Palaniswamy, S.; Chakravarthy, S.; Peroomian, O. Hypersonic Flow Predictions Using Linear and Nonlinear Turbulence Closures. *AIAA Journal of Aircraft* **July/August 2000**, *37* (4), 671–675.

12. Goldberg, U.; Peroomian, O.; Chakravarthy, S. *Application of the k-ε-R Turbulence Model To Wall-Bounded Compressive Flows*; AIAA 98-0323; January 1998.

13. Hirsch, C. *Lessons Learned from the First AIAA-SWBLI Workshop CFD Simulations of Two Test Cases*; AIAA 2010-4824, June/July 2010.

14. Lapsa, A. P.; Dahm, W.J.A. Stereo Particle Image Velocimetry Of Nonequilibrium Turbulence Relaxation In A Supersonic Boundary Layer. *Experiments in Fluids* **June 2010**, *50*, 89–108, Springer-Verlag.

15. Menter, F. R. Influence of Freestream Values on k-ω Turbulence Model Predictions. *AIAA Journal* **1992**, *30* (6), 1657–1659.

16. Menter, F. R. Two-Equation Eddy-Viscosity Turbulence Models for Engineering Applications. *AIAA Journal* **August 1994**, *32* (8), 1598–1605.

17. Menter, F. R. *Zonal Two-Equation k-ω Turbulence Models for Aerodynamic Flows*; AIAA 93–2906; July 1993.

18. Metacomp Technologies, Inc., "CFD++ User Manual," Agoura Hills, CA, 2007.

19. Settles, G. S.; Dodson, L. J. Supersonic and Hypersonic Shock/Boundary-Layer Interaction Database. *AIAA Journal* **July 1994**, *32* (7), 1377–1383.

20. Spalart, P. R. *Trends in Turbulence Treatments*; AIAA 2000–2306; June 2000.

21. Spalart, P. R.; Allmaras, S. R. A One-equation Turbulence Model for Aerodynamic Flows. *Recherche Aerospatiale* **1994**, No 1, 5–21.

22. Spalart, P. R.; Rumsey, C. L. Effective Inflow Conditions for Turbulence Models in Aerodynamic Calculations. *AIAA Journal* **October 2007**, *45* (10), 2544–2553.

List of Symbols, Abbreviations, and Acronyms

AFRL	U.S. Air Force Research Laboratory
APG	Aberdeen Proving Ground
ARL	U.S. Army Research Laboratory
CCAS	Collaborative Center for Aeronautical Sciences
CFD	computational fluid dynamics
CKE	cubic k-ε
DoD	Department of Defense
DSRC	DoD Supercomputing Resource Center
HLLC	Harten-Lax-van Leer-Contact
IUSTI	Institut Universitaire des Systèmes Thermiques Industriels Wind Tunnel
KER	k-ε-R
LES	Large Eddy Simulation
PIV	particle image velocimetry
RANS	Reynolds-averaged Navier-Stokes
RKE	realizable k-ε
RSM	Reynolds Stress Transport
RT	R_t
SA	Spalart-Allmaras
SBLI	shock-boundary layer interaction
SPIV	Stereo-PIV
SST	Shear Stress Transport
TVD	Total-Variation-Diminishing
UMICH	University of Michigan Wind Tunnel

NO. OF COPIES	ORGANIZATION
1 (PDF only)	DEFENSE TECHNICAL INFORMATION CTR DTIC OCA 8725 JOHN J KINGMAN RD STE 0944 FORT BELVOIR VA 22060-6218
1	DIRECTOR US ARMY RESEARCH LAB IMNE ALC HRR 2800 POWDER MILL RD ADELPHI MD 20783-1197
1	DIRECTOR US ARMY RESEARCH LAB RDRL CIO LL 2800 POWDER MILL RD ADELPHI MD 20783-1197
1	DIRECTOR US ARMY RESEARCH LAB RDRL CIO MT 2800 POWDER MILL RD ADELPHI MD 20783-1197
5	RDECOM ARDEC RDAR MEF E D CARLUCCI M DUCA B ELLIS I MEHMEDAGIC B WONG BLDG 94 PICATINNY ARSENAL NJ 07806-5000
1	RDECOM ARDEC RDAR MEF E C KESSLER BLDG 3022 PICATINNY ARSENAL NJ 07806-5000
6	RDECOM ARDEC RDAR MEM A S CHUNG G MALEJKO T RECCHIA W SU W TOLEDO E VAZQUEZ BLDG 94S PICATINNY ARSENAL NJ 07806-5000

NO. OF COPIES	ORGANIZATION
1	RDECOM ARDEC RDAR WSW F L FLORIO BUILDING 8 PICATINNY ARSENAL NJ 07806-5000
3	RDECOM ARDEC RDAR MEM A A FARINA S HAN C WILSON BLDG 95 PICATINNY ARSENAL NJ 07806-5000
1	RDECOM ARDEC RDAR WSW F D CLER 215 BUCKTHORN DR COATESVILLE PA 19320
4	RDECOM AMRDEC RDMR SSM A L AUMAN C MIKKELSEN K KENNEDY E VAUGHN REDSTONE ARSENAL AL 35898-5252
1	AIR FORCE RESEARCH LABORATORY J BENEK 2210 EIGHTH ST BLDG 146 RM 225 WRIGHT-PATTERSON AFB OH 45434
1	AIR FORCE RESEARCH LABORATORY AFRL RW J DUDLEY 101 WEST EGLIN BLVD EGLIN AFB FL 32542
2	NASA GLENN RES CENTER J DEBONIS N GEORGIADIS 21000 BROOKPARK RD CLEVELAND OH 44135
2	NAWCWD R SCHULTZ P CROSS 1900 N KNOX ROAD M/S 6622 CHINA LAKE CA 93555

NO. OF COPIES	ORGANIZATION
1	NAVAIR J LEE SUITE 1320-D3 48110 SHAW ROAD UNIT #5 PATUXENT RIVER MD 20670
1	SAIC D HALL 1150 FIRST AVE STE 400 KING OF PRUSSIA PA 19406
1	ALLIANT TECHSYSTEMS INC R H DOHRN MN07 MN14 4700 NATHAN LN PLYMOUTH MN 55442

ABERDEEN PROVING GROUND

26	DIR USARL RDRL WM P PLOSTINS RDRL WML M ZOLTOSKI J NEWILL RDRL WML A W OBERLE L STROHM RDRL WML D J SCHMIDT M NUSCA RDRL WML E V BHAGWANDIN (3 CPS) I CELMINS G COOPER J DESPIRITO L FAIRFAX F FRESCONI J GARNER B GUIDOS K HEAVEY G OBERLIN J SAHU S SILTON P WEINACHT RDRL WML F D LYON J MALEY RDRL VTV R SINGH M FLOROS

NO. OF COPIES	ORGANIZATION
1	AFOSR EOARD G ABATE 86 BLENHEIM CRESCENT RUISLIP MIDDLESEX HA4 7HB UNITED KINGDOM
1	UNIVERSITY OF CAMBRIDGE DEPT OF ENGINEERING H BABINSKY TRUMPINGTON ST CAMBRIDGE CB2 1PZ UNITED KINGDOM
1	NUMECA INTL C HIRSCH AV LEOPOLD WIENER 87 BRUSSELS 1170 BELGIUM
3	DEFENCE RESEARCH AND DEVELOPMENT CANADA – VALCARTIER F LESAGE N HAMEL R PIMENTEL 2459 PIE-XI BLVD NORTH VAL-BELAIR (QC) G3J1X5 CANADA
3	DSTL PORTSDOWN WEST R CHAPLIN T BIRCH B SHOESMITH LEVEL D, EAST COURT PORTSDOWN HILL ROAD FAREHAM P017 6AD UNITED KINGDOM
1	DSTO G MCKENZIE 506 LORIMER STREET FISHERMANS BEND VIC 3207 AUSTRALIA